Chemical Engineering Journal 452 (2023) 139598

Contents lists available at ScienceDirect

Chemical Engineering Journal

journal homepage: www.elsevier.com/locate/cej

Using Au NPs anchored on ZrO_2/carbon black toward more efficient H_2O_2 electrogeneration in flow-by reactor for carbaryl removal in real wastewater

Matheus S. Kronka *, Guilherme V. Fortunato, Leticia Mira, Alexsandro J. dos Santos, Marcos R. V. Lanza *

São Carlos Institute of Chemistry, University of São Paulo, Avenida Trabalhador São-Carlense 400, São Carlos, SP 13566-590, Brazil

ARTICLE INFO

Keywords:
Hybrid carbon-based support
Gold nanoparticles
Electrochemical advanced oxidation process
Carbaryl removal
Urban wastewater

ABSTRACT

In the present study, we designed a highly efficient catalyst for H_2O_2 production using gold nanoparticles (Au NPs) anchored on hybrid substrate composed of ZrO_2 and Printex L6 carbon (Au-ZrO_2/PL6C). The higher selectivity of Au-ZrO_2/PL6C (97%) toward H_2O_2 electrogeneration and its improved activity in terms of ORR onset potential (140 mV for more positive values) compared to Au/PL6C (80%) were attributed to the synergism between Au NPs anchored on ZrO_2/PL6C hybrid support. The results obtained from the application of the catalysts for H_2O_2 generation on gas diffusion electrode (GDE) after 120 min of electrolysis reflected the following order of efficiency: PL6C (~140 mg L^{-1}) < ZrO_2/PL6C (~235 mg L^{-1}) < Au/PL6C (~374 mg L^{-1}) < Au-ZrO_2/PL6C (~600 mg L^{-1}). Given that Au-ZrO_2/PL6C exhibited the highest catalytic efficiency, this catalyst was employed for the removal of carbaryl (CBR) using different electrochemical advanced oxidation processes. The CBR degradation tests exhibited pseudo first-order kinetics, with the electro-Fenton (EF) and photoelectro-Fenton (PEF) processes recording the fastest removal kinetics (3.5×10^{-2} s^{-1} and 4.1×10^{-2} s^{-1}, respectively). The PEF process exhibited the highest efficiency in terms of organic by-products mineralization; this was attributed to the additional photodecarboxylation of the Fe(III)-RCOOH complexes by UVC light. The aromatic by-products, short chain carboxylic acids, and ionic nitrogen species produced during the mineralization process contributed to the successful degradation of CBR. Apart from the analysis with synthetic water, the study also analyzed the treatment of urban wastewater spiked with CBR using a pre-pilot flow plant.

1. Introduction

The increasingly growing global demand for food caused by the dramatic rise in human population over the last 50 years has generated the need for massive production of food, and this has led to the expansion of agricultural production worldwide [1]. The expansion of agricultural activities has also given rise to widespread use of pesticides which have become indispensable for ensuring the large-scale production of food with high quality through the prevention and control of various pests and disease carriers as this contributes toward enhancing agricultural production by reducing crop losses and increasing crop yields without expanding the planted field [1,2]. According to the Food and Agriculture Organization of the United Nations (FAO), the annual global consumption of pesticides between 2010 and 2019 was >4 million tons (on average), with China, USA and Brazil accounting for over 60% of the total amount of pesticides consumed worldwide [3]. Despite the aforementioned benefits of pesticides, their chemical compositions contain hazardous compounds, and as such, their rampant application in agricultural production has contributed significantly toward an increase in the contamination of water bodies (through leaching, erosion, and so forth) and environmental pollution worldwide. In fact, several studies reported in the literature have detected the presence of pesticides in groundwater, wastewater, surface water and tap water at concentrations ranging from 10 to 4,000 ng L^{-1} on average [4,5]. Owing to the hazardous compounds present in pesticides, exposure to these pollutants through water bodies has been found to be extremely toxic and these compounds can potentially act as endocrine disruptors even at very low concentrations. Bearing that in mind, over the last decades, there has been a considerable interest among researchers in the development of highly effective techniques for the treatment of water and

* Corresponding authors.
E-mail addresses: mskonka@usp.br (M.S. Kronka), marcoslanza@usp.br (M.R.V. Lanza).

https://doi.org/10.1016/j.cej.2022.139598
Received 30 May 2022; Received in revised form 30 September 2022; Accepted 2 October 2022
Available online 8 October 2022

wastewater containing harmful pollutants [6–8].

Electrochemical advanced oxidation processes (EAOPs) are a highly promising technology which has been proven to be suitable for application in water and wastewater treatment. Among the wide range of EAOPs reported in the literature, anodic oxidation (AO) is the most commonly applied technique. In the AO process, organic pollutants are oxidized through heterogeneous hydroxyl radicals (•OH) formed on the surface of non-active anodes (M) after water discharge, as demonstrated in Eq. (1). As it has been extensively reported in the literature, boron-doped diamond (BDD) is the best non-active anode for water treatment due to its excellent electrocatalytic properties [7–11].

Despite the unquestionable popularity of AO, EAOPs based on electrochemical Fenton reactions have been reported to be the most efficient treatment techniques when it comes to the removal of hazardous compounds in water matrices [12,13]. This outstanding efficiency of electro-Fenton (EF) processes lies in the production of homogeneous •OH radicals; these radicals are generated from the activation of H_2O_2 using Fe^{2+} ions via the classical Fenton reaction (see Eq. (2)). Over the recent years, the technological advances made in the homogeneous production of •OH have sparked the interest of researchers in electro-Fenton processes due to the facilitated mechanism involving the electrochemical production of H_2O_2 from the selective 2-electron oxygen reduction reaction (ORR) using carbon-based catalysts configured as gas diffusion electrodes (GDE) [12–18]. Furthermore, the use of abundant, stable, and low-cost materials for the electrochemical production of H_2O_2 via inorganic metal-oxide photoanodes has also gained considerable traction among researchers in the field [19].

$$M + H_2O \rightarrow M(^{\bullet}OH) + H^+ + e^- \quad (1)$$

$$Fe^{2+} + H_2O_2 + H^+ \rightarrow Fe^{3+} + {}^{\bullet}OH + H_2O \quad (2)$$

Studies reported in the literature show that carbonaceous catalysts have been widely employed in the composition of porous cathodes for H_2O_2 production thanks to their abundant availability, low cost, and high selectivity for ORR via $2e^-$ [20–24]. However, the poor electrochemical activity of carbon-based catalysts makes their application in large-scale H_2O_2 production unfeasible [25–28]. In view of that, the use of noble metal-based materials has gained enormous traction among researchers since these metals facilitate charge transfer and this helps enhance the activity of carbon catalysts. In addition to providing us with reactivity patterns, density functional theory (DFT) calculations have become an important tool in the interpretation and design of more efficient catalytic systems for H_2O_2 production [29,30]. Thermodynamic analysis based on DFT has shown that gold (Au) and silver (Ag) are among the class of noble metals that do not interact strongly with O_2 and act to facilitate the stabilization of *OOH on metal surfaces - the principal intermediate of ORR when it comes to high selectivity for H_2O_2 production[31–34].

While they are evidently scarce and expensive, noble metals have been proven to be capable of effectively resisting the drastic operating conditions imposed by electrochemical devices and are able to operate for a much longer period compared to non-noble metal-based catalysts. Owing to the scarcity and high costs of noble metals, new strategies have been developed with a view to minimizing the amount of these metals used in the composition of noble metal-based catalysts while preserving or even improving the electrochemical properties of the catalysts [31,32,35,36].

To boost the activity and selectivity for H_2O_2 production while decreasing the noble metal loading in the catalysts, some authors have successfully employed relatively lower amount of noble metals in combination with abundant transition metal (TM) oxides and carbon materials [30,37–39]; these studies have employed different strategies which involved the application of highly oxophilic TM oxides close to nanoparticulate Au, Pd and Au-Pd systems to synergistically enhance catalytic activity and influence the reaction pathway by which ORR will preferentially occur. Although some combination of noble metals with TM oxides and carbonaceous materials has proven to be able to tailor the electrocatalytic activity, selectivity and stability, this class of catalysts can still be further explored for H_2O_2 electroproduction.

Thus, in the present study, we report the development of a novel cathode material based on gold nanoparticles (Au NPs) supported on hybrid substrate composed of ZrO_2 and Printex L6 carbon (ZrO_2/PL6C) and its application for the efficient production of H_2O_2 in wastewater treatment processes. ZrO_2 was used as supporting material for Au NPs due to its catalytic behavior has been widely studied toward the electrochemical production of H_2O_2 and also for its promising electrocatalytic properties found for electrochemical oxidation [40–43]. An advantage of choosing ZrO_2 is that its eco-friendly production via microwave-assisted hydrothermal synthesis on PL6C (ZrO_2/PL6C) carbon matrix has been optimized before [42]. Furthermore, ZrO_2 is a non-toxic and electrochemically stable oxide which presents electronegative and oxophilic characteristics when employed as supporting material for noble metal nanoparticles [44]. The electrochemical characterization of the materials and the analysis of their electrocatalytic properties with respect to oxygen reduction reaction (ORR) were evaluated using a rotating ring-disk electrode (RRDE) system, while the kinetics of H_2O_2 production was investigated using gas diffusion electrode (GDE). The Au-ZrO_2/PL6C catalyst was used as cathode for H_2O_2 production in an electrochemical system coupled with boron-doped diamond (BDD) anode with a view to evaluating the removal of carbaryl pesticide using different EAOPs. Carbaryl has been classified as an endocrine disruptor present in water sources. The experimental tests targeted at the removal of carbaryl were carried out in a pre-pilot reactor using both synthetic and real wastewater effluents and the Au-ZrO_2/PL6C cathode material [45–47].

2. Experimental

2.1. Reagents

The Printex L6 (PL6C) carbon black pigment was purchased from Evonik do Brasil ltd. The metallic precursor $(ZrO_2)_2CO_2{\cdot}H_2O$ and $HAuCl_4{\cdot}3H_2O$ (99%) were acquired from Alfa Aesar and Sigma Aldrich, respectively. Other reagents employed in the experiments included the following: sulfuric acid (Vetec, 97.8%), isopropyl alcohol (Vetec, 99.5%), potassium sulfate (Sigma-Aldrich, 99%), potassium hydroxide (J. T. Baker, 99%), and 60% v/v dispersion of poly(tetrafluoroethylene) (PTFE - Uniflon). Carbaryl (99%) analytical standard was acquired from Sigma-Aldrich and ion chromatography standards of NH_4^+, N-NO_2^- and N-NO_3^- in 1000 mg L^{-1} solution were obtained from Specsol. The solutions were prepared using ultrapure water from a Milli-Q system with resistivity > 18 MΩ cm at 25 °C.

2.2. Synthesis of ZrO_2/PL6C, Au-ZrO_2/PL6C, and Au/PL6C catalysts

To obtain the hybrid Au-ZrO_2/PL6C, a 2-step hydrothermal synthesis was employed. First, the ZrO_2/PL6C hybrid substrate was synthesized by the microwave-assisted hydrothermal method, as described in reference [42].

In the next step, the hydrothermal syntheses (without microwave assistance) of the Au particles supported on ZrO_2/PL6C (Au-ZrO_2/PL6C) and on pure PL6C (Au/PL6C) were carried out based on the method proposed by Fortunato *et al.* [48] with some adaptations. Briefly, an amount of 32 mg of ZrO_2/PL6C or bare PL6C was dispersed in 20 mL of Milli-Q water; this was followed by the addition of 240 μL of 0.1 mol L^{-1} $HAuCl_4$ aqueous solution and 8.4 mg of Pluronic F-127 (structure directing agent of metallic NPs) into the mixture. The mixture was left in an ultrasonic bath (Soni-top 404A) for 40 min. Afterwards, the solubilized mixture was heated to 100 °C using a hot plate, and an amount of 36.7 mg of ascorbic acid, which had been previously dissolved in 1 mL of ultrapure water, was quickly poured into the mixture. The heating was stopped after 5 min in boiling condition, and the solution was kept under

magnetic stirring for further 2 h until the Au particles were stabilized on the supporting material, leading to the formation of the Au/PL6C and Au-ZrO_2/PL6C composites. After reaching room temperature, the precipitates containing the composites formed were washed by centrifugation 10 times with Milli-Q water to remove the surfactant and were then dried in an oven at 80 °C overnight.

2.3. Physical-chemical characterization methods

The physical-structural characterization of the catalysts was initially performed using scanning electron microscopy (SEM) and transmission electron microscopy (TEM). The SEM analyses were performed using a Jeol JSM Microscope model 7500F. To perform the TEM and scanning-TEM (STEM) analyses, an amount of 3 μL of a diluted dispersion of the catalyst powder was dripped onto a 300-mesh copper TEM grid covered with carbon film (Electron Microscopy Sciences). The TEM and STEM images were recorded using a JEOL JEM2100 LaB_6 HRTEM or a FEI TECNAI G^2 F20 HRTEM microscope operating at 200 kV. For the determination of the loading of metals present in the samples, 2–5 mg amounts of the materials were placed inside a thermogravimetric analyzer TGA-50 (Shimadzu) in FID 5.0 synthetic air at a flow rate of 50 mL min^{-1} and the analysis was performed under the heating rate of 10 °C min^{-1} with the temperature ranging from 25 and 900 °C. Energy dispersive X-ray spectroscopy (EDS) analyses were performed in order to define the proportions of Au and Zr in the catalyst samples. The materials were placed on fluorine tin oxide plates (FTO, FlexiTec Organic Electronics) with 1.0 cm × 1.0 cm × 0.1 cm dimension and subjected to EDX analyses using ThermoNoran System Six apparatus.

The analysis of the surface of the catalysts was performed by X-ray photoelectron spectroscopy (XPS) using ESCA Scienta Omicron spectrometer operating under the following conditions: Al/Ka radiation: 1,486.6 eV; potential: 15 kV; current density: 15 mA; and power: 225 W. The survey spectra were recorded using pass energy of 50 eV with interval of 1 eV while the high-resolution spectra were recorded using pass energy of 10 eV with interval of 0.1 eV. The Shirley method was used to subtract the inelastic noise from the high-resolution spectra of Au 4f, Zr 3d, C 1 s and O 1 s. The narrow spectra were deconvoluted according to a Voigt-type function with Gaussian (70%) and Lorentzian (30%) combinations using the Casa XPS® software.

2.4. Thin film layer analysis in RRDE system

Initially, the catalyst dispersion was prepared in a ratio of 2 mg of catalyst to 1 mL of water/isopropanol dispersant (50/50 v/v) using an ultrasonic bath. The microlayer was prepared on glassy carbon disk electrode (geometric area = 0.2475 cm^2) by drop casting 25 μL of the dispersion. After the evaporation of the solvent with the aid of N_2 flow, a thin film layer containing catalyst loading of 200 μg cm^{-2} was obtained.

The electrochemical assays were performed in a three-compartment benchtop cell using 150 mL of 0.1 mol L^{-1} K_2SO_4 electrolyte at pH = 2.5 (adjusted with H_2SO_4). The working electrode employed was a Pine E7R9 rotating ring-disk electrode (RRDE) composed of a glassy carbon disk and platinum ring (geometric area = 0.1866 cm^2); Ag/AgCl (KCl 3 mol L^{-1}) was used as reference electrode and a 240 mm^2 platinum plate was employed as counter electrode. The assays were performed using Metrohm Autolab PGSTAT-302 N bi-potentiostat.

The analysis of the catalysts was conducted by cyclic voltammetry (CV) using O_2-saturated electrolyte and N_2 deaerated solution in the potential range of 1.4 to −0.6 V vs. Ag/AgCl and at scan rate of 50 mV s^{-1}. The ORR activity was investigated in a hydrodynamic system using linear sweep voltammetry (LSV) in the potential range of 0.6 to −0.8 V vs. Ag/AgCl (in the disk) and at scan rate of 5 mV s^{-1}. The working electrode was kept at 900 rpm. To monitor the presence of H_2O_2 during the assay, a constant potential of 1.0 V was applied to the ring. The analysis of the catalyst selectivity toward H_2O_2 production was performed based on Eq. (3) below [49]:

$$S_{H2O2} = \frac{2i_q/N}{i_d + i_q/N} \times 100 \quad (3)$$

where i_a represents the current from the ring electrode (in amperes (A)), i_d refers to the current observed in the disk electrode (A), and N is the collection number provided by the manufacturer of the RRDE (PINE - N = 0.37). The equation is multiplied by 100 to obtain S_{H2O2} in % terms.

The accelerated stress test (AST) was used to evaluate the long-term electrochemical stability of the gold-based catalysts. The technique consisted of evaluating both the cyclic profile of the materials and their catalytic activity in ORR using LSV tests before and after applying 5000 CVs in the potential range of 0.4–1.0 V vs RHE in 0.1 mol L^{-1} K_2SO_4 solution (at pH 2.5) saturated with O_2 and scan rate of 500 mV s^{-1}.

2.5. H_2O_2 accumulation assays in gas diffusion electrodes

To produce the GDE, a catalytic mass was prepared in the ratio of 40% (w/w) of PTFE / Printex L6 carbon, as reported in the literature [50]. Initially, an amount of 1.2 g of catalyst mass was scattered over 120 cm^2 PX30-PW03 carbon cloth (purchased from Plain Weave Fabric) and transferred to a metal support. The unmodified GDE (of 10 mg cm^{-2}) was produced in a thermostat hydraulic press under the following conditions: temperature: 270 °C; weight: 0.5 ton; and time: 15 min. The modified GDE was prepared by drop casting 40 mg catalysts solution - produced using 40% PTFE (w/w), on the unmodified GDE, and this yielded a catalyst loading of 200 mg cm^{-2}. The production of H_2O_2 was tested in a laboratory scale and in a pre-pilot plant with electrochemical flow reactor in recirculation mode under the following conditions:

Laboratory scale: The performance of PL6C, ZrO_2/PL6C, Au/PL6C and Au-ZrO_2/PL6C in terms of H_2O_2 electrogeneration was evaluated by applying a current density (j) of 50 mA cm^{-2} in 150 mL synthetic medium under controlled O_2 flow rate (100 mL min^{-1}). The electrochemical cell employed consisted of GDE – employed as cathode, and BDD – employed as anode, both with a geometric area of 5.0 cm^{-2}.

Pre-pilot plant: The stability of H_2O_2 production was tested in a flow-by electrochemical reactor using Au-ZrO_2/PL6C cathode material with j of 50 mA cm^{-2} in 1.8 L synthetic and real media under recirculating solution at a flow rate of 50 L h^{-1} and controlled O_2 flow rate (100 mL min^{-1}). Here, the area of the GDE and BDD electrodes was scaled to 20 cm^2.

In both systems, the experiments were conducted using Minipa MPS-3005B DC power supply system.

2.6. Treatment of CBR using EAOPs

A comparative degradation/mineralization analysis of 10 mg L^{-1} CBR was performed in a benchtop cell (with 150 mL of 0.1 mol L^{-1} supporting electrolyte) (at pH = 2.5) at fix current density *(j)* of 50 mA cm^{-2} using the following EAOPs: AO, AO-H_2O_2, AO-H_2O_2/UVC, EF and PEF. The EF and PEF treatment processes were performed using 0.25 mmol L^{-1} concentrations of Fe^{2+}. Different parameters were analyzed under the PEF process; the parameters evaluated included current density (j ranging from 25 to 100 mA cm^{-2}) and initial CBR concentration (5.0 to 20.0 mg L^{-1}). A 5 W UVC lamp (Pen-Ray 11SC-2.12 model) was used to illuminate the solution in the PEF process and to perform the CBR photolysis test [35]. Optimized laboratory-scale operating conditions were applied to a pre-pilot plant coupled to a 16 W UVC lamp for the analysis of CBR removal under the PEF process. The tests were carried out for 60 min at 50 mA cm^{-2} using 1.8 L of the following effluents:

- Synthetic effluent: 50 mmol L^{-1} K_2SO_4 in Milli-Q water at pH 2.5 (adjusted with H_2SO_4), with conductivity of 10.5 mS;
- Effluent from sewage treatment plant collected from São Paulo State, Brazil. The physical–chemical composition of the effluent can be

summarized as follows: pH = 7.1; conductivity = 1.5 mS cm^{-1}; total organic carbon (TOC) = 9.2 mg L^{-1}; dissolved solids = 391.0 mg L^{-1}; and turbidity = 29.4 NTU. The ionic species identified were ammonia (NH_4^+) = 5.8 mg L^{-1}, calcium (Ca^+) = 29.7 mg L^{-1}, magnesium (Mg^+) = 5.9 mg L^{-1}, potassium (K^+) = 15.2 mg L^{-1}, sodium (Na^+) = 90.7, chloride (Cl^-) = 31.2 mg L^{-1}, nitrate (NO_3^-) = 9.4 mg L^{-1}, nitrite (NO_2^-) = 1.1 mg L^{-1}, and sulfate (SO_4^{2-}) = 22.4 mg L^{-1}. (Additional K_2SO_4 was added and the pH lowered to 2.5 so that both solutions would have similar conductivity of 10.5 mS).

2.7. Analytical techniques

The quantification of H_2O_2 was performed by UV–vis spectroscopy using 350 nm of H_2O_2 and $(NH_4)_6Mo_7O_{24}$ complex [50,51]. The analysis was carried out using Shimadzu UV-1900 spectrophotometer. Using the amount of H_2O_2 produced, the energy consumption was evaluated based on Eq. (4), while the percentage of current efficiency (CE) was estimated based on the Faraday's law in Eq. (5). See Equations (4) and (5) below:

$$EC\left(kWh\,kg_{H2O2}^{-1}\right) = \frac{i\,E_{cell}t}{m\,1000} \tag{4}$$

$$CE_{H2O2}(\%) = \frac{2\,F\,C_{H2O2}V_s}{i\,t} \times 100 \tag{5}$$

where i represents the current applied (given in amperes (A)), t is the electrolysis time (in hours (h) in Eq. (4) and in seconds (s) in Eq. (5)), E_{cell} stands for electrochemical cell potential (in volts, V), m is the mass of H_2O_2 produced (in kg), 2 refers to the number of electrons involved in the reduction of an oxygen molecule to produce H_2O_2, F stands for the Faraday constant (96,487C mol^{-1}), C_{H2O2} is the concentration of H_2O_2 (in mol L^{-1}), and vs represents the volume of the solution (in L).

The concentration of CBR was monitored by high performance liquid chromatography (HPLC) with the aid of a Shimadzu HPLC device using the stationary phase constituted by a Supelcosil C18 pre-column (4 mm × 3.0 mm i.d.) attached to Phenomenex Luna C18 column (250 × 4.6 mm, 5 μm). A UV detector SPD-20A selected at λ = 220 nm attached to the HPLC system was used to monitor the concentration of CBR [52]. The following conditions were applied for the chromatographic analysis: retention time of carbaryl: 5.45 min in the mobile phase; mobile phase: acetonitrile/water in the ratio 60/40 (v/v); flow rate: 1.0 mL min^{-1}.

The NO_2^-, NO_3^- and NH_4^+ inorganic species were determined by ion exchange chromatography, as described in the literature [53]. The short-chain carboxylic acids were also analyzed by ion exchange chromatography. The separation was performed using Metrosep C4 column (150 mm/4.0 mm) and Metrosep C4 Guardian/4.0 pre-column at 30 °C. The elution of the small chain acids was performed using 1.7 mmol L^{-1} nitric acid/0.7 mmol L^{-1} dipicolinic acid at flow rate of 0.9 mL min^{-1}. The analytical curves of the carboxylic acids were constructed in the concentration range of 0 to 100 mg L^{-1} ($R^2 > 0.99$) using the following standards: acetic acid (t_r = 3.90 min), formic acid (t_r = 4.40 min), succinic acid (t_r = 14.8 min), oxalic acid (t_r: 17.2 min), and fumaric acid (t_r = 22.9 min).

The mineralization of total organic carbon (TOC) was monitored by Shimadzu TOC-VCPN equipment; the mineralization was calculated using Eq. (6) below:

$$TOC\,mineralization\,(\%) = \frac{TOC_0 - TOC_f}{TOC_0}\,x\,100 \tag{6}$$

All samples were pre-filtered using chromafilXtra PET-45/25 0.45 μm filters. The amount of energy consumed (EC) in CBR mineralization recorded under each EAOPs was calculated based on Eq. (7) below using the TOC values:

$$EC\left(kWh\,kg^{-1}\right) = \frac{E_{cel}\,I\,t}{\Delta TOC\,1000} \times 100 \tag{7}$$

where I stands for current (A), E_{cel} is the cell potential (V), and ΔTOC is the mass of TOC removed (kg) over time.

3. Results and discussion

3.1. Physical-chemical characterization of the catalysts

Au particles were grown on bare PL6C and on the ZrO_2-PL6C synthesized hybrid material (its surface and physical properties have been described in a previous study [42]) by the hydrothermal reduction approach. The Au particles on the substrate were produced from the reduction of Au^{3+} ions by citric acid, which is typically used in synthesis processes as a reducing agent [54]. The difficulty involved in the production of Au nanoparticles lies in being able to produce small and widely distributed particles on the substrate so as to maximize the use of the metal in the catalyst and avoid the formation of large-sized particles or large metal agglomerates. In this sense, the physicochemical characteristics of the support material, such as active surface area, presence of functional groups, heteroatoms and defects, can have a direct influence on the interaction between the metal and the support material; in addition, these characteristics of the support material are also found to play a crucial role in some properties of the nanoparticle such as the distribution of the metal in the support material, the particle size, as well as the chemical attachment and stability [48,55–59]. In this context, the present study sought to evaluate the application of PL6C and ZrO_2/PL6C as supporting materials for Au nanoparticles (Au NPs) and the effects of these materials on the electrochemical catalysis of ORR targeted at the production of H_2O_2 in acid media.

Initially, the Au/PL6C and Au-ZrO_2/PL6C catalysts were characterized by field emission scanning electronic microscopy (FE-SEM), transmission electronic microscopy (TEM), scanning TEM (STEM), high-resolution TEM (HR-TEM), and selected area electron diffraction (SAED) pattern, as shown in Fig. 1a-g and S1. FE-SEM (Fig. 1a) and TEM (Fig. S1a) images recorded for Au/PL6C showed the catalyst characterized by the presence of Au particles with size of 186.7 nm (on average) which were poorly dispersed on the PL6C matrix. The HR-TEM image (Fig. 1b) obtained for the Au/PL6C catalyst showed the Au particles with nanometer dimensions, as reported in the literature [21]. In addition, the lattice fringes with distances of ca. 0.21 and 0.23 nm can be seen, which are typically related to the planes (200) and (111) for face-centered cubic structures (*fcc*) of Au [39]. The selected area diffraction (SAED) pattern image (Fig. 1c) obtained for the Au/PL6C catalyst revealed the presence of polycrystal structures with (111), (200), (222) and (311) orientations. According to the literature, these diffraction patterns correspond to the polycrystalline structure of Au in the catalyst [60,61].

Clearly different from what was observed in the Au/PL6C catalyst, the FE-SEM, STEM, and HR-TEM images of the Au-ZrO_2/PL6C (Fig. 1d-f and Fig. S1c-f) showed the presence of nanometric structures with predominantly icosahedral and dodecahedral shapes widely distributed on the substrate. The Au nanoparticles in the Au-ZrO_2/PL6C catalyst were ca. 77 nm on average (see Fig. S1c); this is roughly 2.5 times smaller than the size of the Au particles in the Au/PL6C catalyst. Interestingly, after a careful inspection of the STEM, dark-field STEM and HR-TEM images obtained for the Au-ZrO_2/PL6C sample (Fig. 1e,f and S1), we found that the Au NPs were anchored on top of the ZrO_2 NPs; this was clearly evident because the ZrO_2 NPs can be easily identified in the HR-TEM image (Fig. 1f) by the presence of lattice fringes measuring 0.29 nm, which are known to be typically characteristic of the *d*-spacing of cubic crystalline structure of zirconia [42]. The energy dispersive X-ray spectroscopy (EDX) elemental mappings of C, O, Au, and Zr obtained for the Au-ZrO_2/PL6C catalyst (Fig. S2 and S3) also indicated that Au and Zr were very close to each other, and both were found to be well dispersed on the carbon-based matrix. However, the SAED image of the Au-ZrO_2/PL6C catalyst (Fig. 1g) showed a diffraction pattern with mostly crystalline characteristics that corresponded to polycrystalline Au; this was similar to the SAED pattern observed for the Au/PL6C catalyst. The

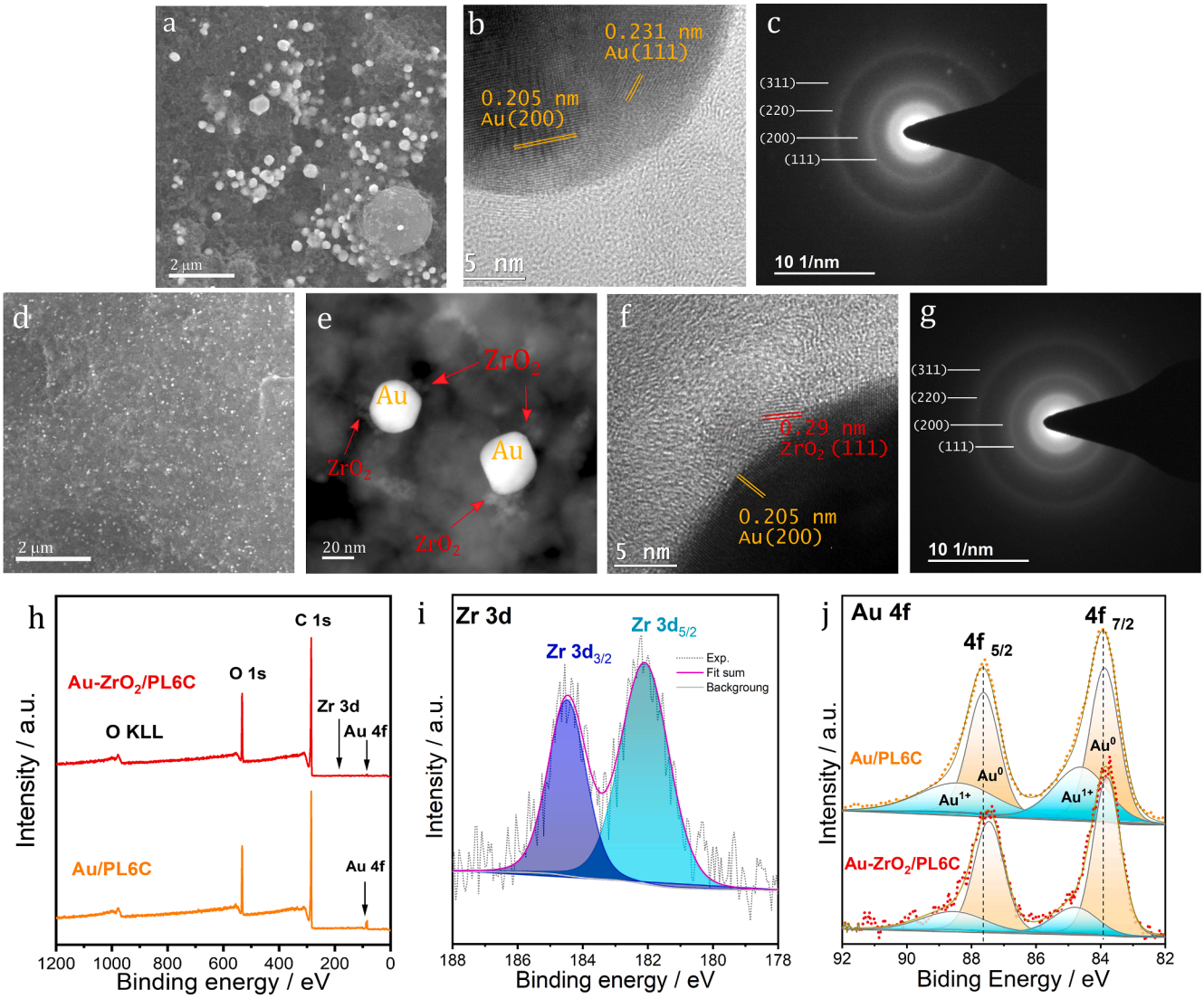

Fig. 1. FE-SEM, HR-TEM, and SAED images for the (a,b,c) Au/PL6C and FE-SEM, dark-field STEM, HR-TEM, and SAED images for (d,e,f,g) Au-ZrO_2/PL6C catalysts, respectively. (h) Survey XPS spectra for Au/PL6C and Au-ZrO_2/PL6C catalysts. (i) High resolution XPS spectrum in Zr 3d region for Au-ZrO_2/PL6C. (j) High resolution XPS spectra recorded in the Au 4f region for Au/PL6C and Au-ZrO_2/PL6C catalysts.

overlap of the larger Au NPs in the small-size ZrO_2 NPs may be a reason for the absence of the Zr diffraction pattern in the Au-ZrO_2/PL6C catalyst. Furthermore, it is relevant to mention that reducing the Au-ZrO_2/PL6C catalyst synthesis procedure from 2 steps (using microwave-assisted hydrothermal method combined with a hydrothermal reduction step) to only one step (single microwave-assisted hydrothermal approach) leads to less dispersion and the formation of Au particles with larger sizes in comparison to Au-ZrO_2/PL6C catalyst produced by 2-step synthesis procedure (c.f. Figs. 1, S1, S2, S3 and S4).

XPS analyses were performed in order to evaluate the surface chemical state of the synthesized Au-modified catalysts. The XPS survey spectrum of the Au/PL6C sample (Fig. 1h) showed the presence of peaks which corresponded to C 1s (284.5 eV), O 1s (532.6 eV), and Au 4f (85.5 eV), while the spectrum of Au-ZrO_2/PL6C exhibited in addition a small peak at 184.5 eV, which is typically attributed to the Zr 3d core level. These survey spectra rule out the presence of any other metallic impurities in both samples. The Zr 3d core-level high-resolution spectrum obtained for Au-ZrO_2/PL6C (Fig. 1i) displayed the presence of the doublet $3d_{3/2}$ and $3d_{5/2}$ due to the spin–orbit splitting at the binding energies of 184.3 and 181.9 eV, respectively, which is a binding energy range commonly associated with the Zr^{4+} oxidation state of zirconium oxide [42]. The spin–orbit components $4f_{7/2}$ and $4f_{5/2}$ can be observed at ca. 84 and 88 eV in the Au 4f core-level spectra of the Au/PL6C and Au-ZrO_2/PL6C samples (Fig. 1j); both peaks can be found to be deconvoluted into two smaller peaks each at 83.8, 84.8, 87.5, and 88.6 eV corresponding to the Au^0 $4f_{7/2}$, Au^{1+} $4f_{7/2}$,Au^0 $4f_{5/2}$, and Au^{1+} $4f_{5/2}$ oxidation states. In fact, the Au^+ species found in both XPS spectra for Au/PL6C and Au-ZrO_2/PL6C samples can be explained by the partial charge transfer from the Printex L6 carbon basic groups (i.e., ketones and quinones) to the supported gold particles, as described in the literature [21,62]. In addition, as pointed out in the literature, small metal particle sizes are expected to have a higher surface energy, which is yet another factor that contributes to the existence of superficially oxidized gold particles [63]. It is worth noting however that although there appeared to be a close similarity between the spectra of the Au/PL6C and Au-ZrO_2/PL6C samples, a careful inspection of the catalysts spectra showed that the ratio of Au^{+1}/Au^0 intensities was 2-fold higher in Au/PL6C compared to Au-ZrO_2/PL6C (even though this catalyst exhibited a smaller particle size); this shows that the presence of ZrO_2 nanoparticles in the hybrid support (a less electronegative species than Au) helped supply electrons and favor the metallic state of Au. Furthermore, a comparative analysis of the Au 4f core-level spectra of

the Au/PL6C and Au-ZrO_2/PL6C catalysts pointed to a slight shift of 0.1 eV to lower binding energy values when ZrO_2/PL6C was used as supporting material instead of pure PL6C; this result shows that the presence of oxophilic Zr exerts an influence over the electronic band structures of Au particles. It should be noted that the changes that occur in the electronic state of Au may lead to changes in the catalytic behavior of the material [30,64–67].

The metal loading in the ZrO_2/PL6C, Au/PL6C and Au-ZrO_2/PL6C carbon-based materials was evaluated using the TGA mass loss analysis shown in Fig S5. The Au/PL6C and Au-ZrO_2/PL6C catalysts recorded similar metal loadings: ~12.7 wt% and ~12.8 wt%, respectively. The results obtained from the EDS analysis helped distinguish the Zr species from the Au species in the Au-ZrO_2/PL6C catalyst; the EDS analysis revealed the following: ~9 wt% Au loading and ~ 4 wt% Zr loading - see Table S1. Thus, based on the results obtained, one will observe that the bimetallic catalyst material also exhibited lower gold loading compared to the zirconium-free material. In general, the use of the ZrO_2/PL6C hybrid support contributed to the production of carbon-based catalyst of gold NPs with small particle size which were uniformly distributed on the substrate. A thorough analysis was conducted in order to evaluate the electrochemical behavior of the synthesized catalysts and H_2O_2 electrogeneration using rotating ring-disk electrode (RRDE) and GDE.

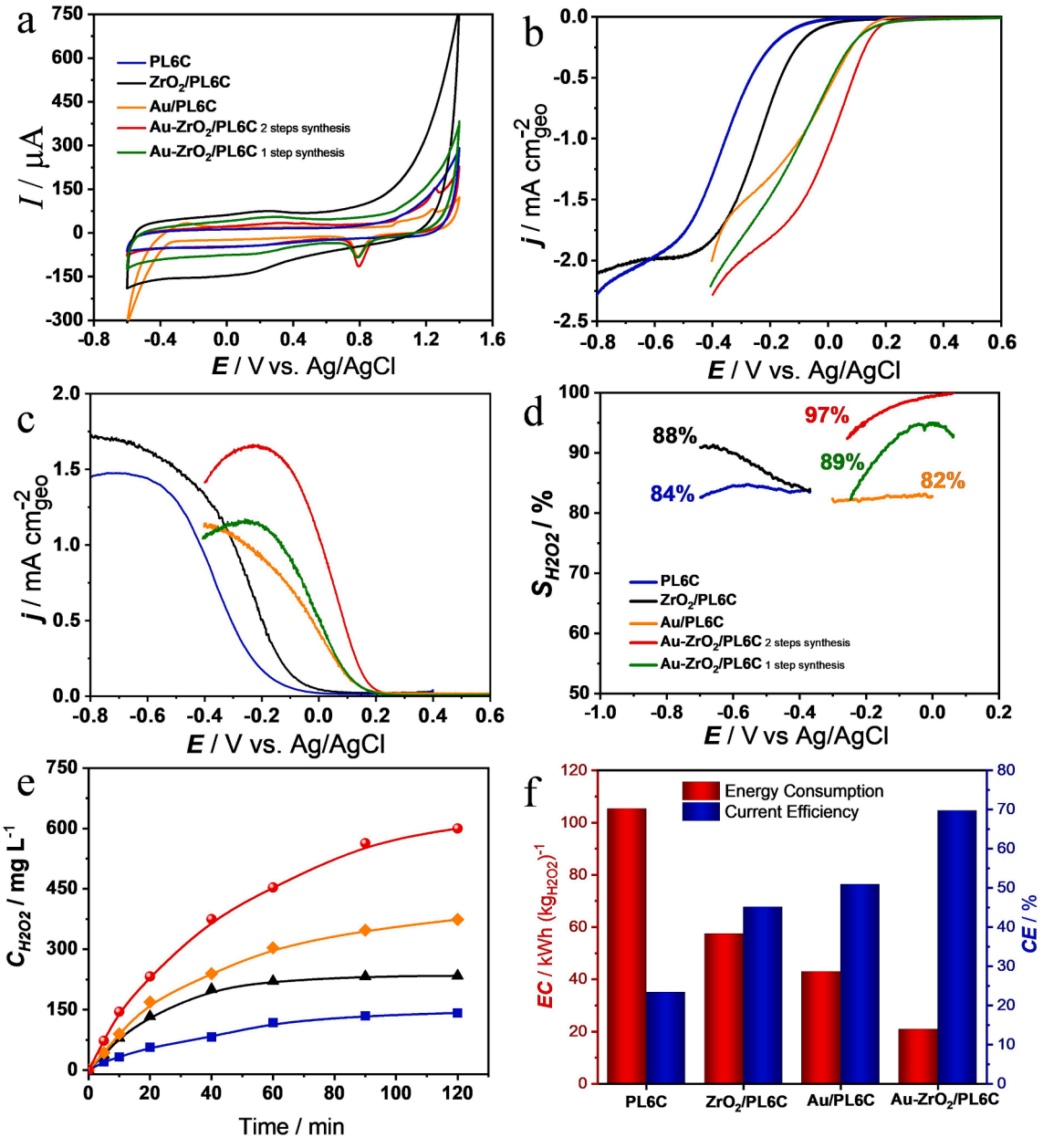

Fig. 2. Electrochemical analysis of the GC disk (RRDE system) modified with PL6C, ZrO_2/PL6C, Au/PL6C and Au-ZrO_2/PL6C catalysts. (a) Cyclic voltammograms obtained at 50 mV s^{-1}, with the application of 150 mL using N_2 bubbling to deaerate 0.1 mol L^{-1} K_2SO_4 solution (at pH 2.5). Linear sweep voltammetry curves of the (b) disk and (c) Pt ring electrodes obtained in a RRDE configuration at scan rate of 5 mV s^{-1} and rotation of 900 rpm, using O_2-saturated solution of 0.1 mol L^{-1} K_2SO_4 at pH 2.5 (the abscissa of Fig. 2C refers to the applied potential at the disk electrode). (d) Selectivity toward H_2O_2 production as a function of applied potential. (e) Capacity of H_2O_2 accumulation during electrolysis at 50 mA cm^{-2} for 120 min in 0.1 mol L^{-1} K_2SO_4 (pH = 2.5) based on the application of GDE modified with PL6C, ZrO_2/PL6C, Au/PL6C and Au-ZrO_2/PL6C and using BDD as anode. (f) Current efficiency (CE) and energy consumption (EC) values obtained from H_2O_2 electrogeneration tests performed for the PL6C, ZrO_2/PL6C, Au/PL6C and Au-ZrO_2/PL6C catalysts.

3.2. Electrocatalytic performance of the materials applied for ORR aimed at H_2O_2 production

The cyclic voltammetric (CV) profiles obtained for the glassy carbon (GC) electrodes modified with PL6C, ZrO_2/PL6C, Au/PL6C or Au-ZrO_2/PL6C catalysts recorded at 50 mV s^{-1} using N_2 bubbling to deaerate 0.1 mol L^{-1} K_2SO_4 solution at pH 2.5 are shown in Fig. 2a. The CV profile of the PL6C-modified GC electrode exhibited mainly capacitive currents and quinone/hydroquinone redox couple centered at ca. 0.3 V vs Ag/AgCl, which are features typically observed for carbon materials in acidic solutions [21,68]. After the incorporation of zirconium oxide into the carbon matrix (ZrO_2/PL6C-modified GC electrode), the non-faradaic currents were drastically increased due to the formation of porous ZrO_2 nanostructures which were widely dispersed on the PL6C. In a previous work, we showed that the presence of ZrO_2 nanostructures in PL6C matrix led to an increase in the electrochemically active surface area (*ECSA*) from 85.6 to 128.2 m^2 g^{-1}, and this led to an increase in the capacitive current of the ZrO_2/PL6C material [42]. In general, the CV profiles of the catalysts containing Au particles (Au/PL6C and Au-ZrO_2/PL6C) exhibited a decrease in capacitive currents due to the incorporation of the metal in the surface of the supporting material, which led to a decrease in the surface area of the carbon catalyst [69]. In addition, one can observe the presence of faradaic peaks related to the formation and reduction of gold oxide species (AuO_x) on the catalyst surface at the potentials of ca. 1.1 and 0.8 V vs Ag/AgCl, respectively [31,70]. It is worth noting that the presence of ZrO_2 in Au-/PL6C (Au-ZrO_2/PL6C) caused a significant shift in the onset potential of the H_2 evolution (at ca. −0.35 V vs Ag/AgCl) to potential values that were more negative than −0.6 V vs Ag/AgCl, which typically competes with ORR when noble metals are employed at high overpotential [71].

The electrochemical analyses of ORR activity and selectivity of the catalysts were carried out by linear sweep voltammetry (LSV) using a rotating ring-disk electrode (RRDE) in O_2-saturated solution of 0.1 mol L^{-1} K_2SO_4 at pH 2.5. The LSV curves obtained for the disk and ring electrodes are shown in Fig. 2b and 2c, respectively. As expected, the LSV curves for the disk electrode showed that the gold-based catalysts (Au/PL6C and Au-ZrO_2/PL6C synthesized in one and two steps) were more active in O_2 reduction compared to the PL6C and ZrO_2/PL6C substrates. However, a careful comparison of the Au/PL6C and Au-ZrO_2/PL6C catalysts showed that the ORR onset potential of Au-ZrO_2/PL6C produced via two-step synthesis procedure was 140 mV more positive than that of Au/PL6C and Au-ZrO_2/PL6C produced by one-step synthesis procedure. This anticipation of ORR points to the synergistic effect of the presence of ZrO_2 in the supporting material on the catalytic activity toward oxygen reduction. The Au-ZrO_2/PL6C catalyst exhibited a higher ORR activity even when the Au loading was about 25% lower in comparison to Au/PL6C (c.f. Table S1). The LSV curves of the ring electrodes (Fig. 2c) displayed the fraction of H_2O_2 produced during the oxygen reduction occurring on the disk as a function of the applied potential. In general, the LSV curves of the ring electrodes showed that the PL6C, ZrO_2/PL6C, Au/PL6C and Au-ZrO_2/PL6C materials were all highly selective for H_2O_2 production, and that the onset potentials for H_2O_2 generation coincided exactly with the ORR onset potentials of the disk electrodes. Based on the LSV curves of the disk and ring electrodes, we calculated the values related to the selectivity of the catalysts toward H_2O_2 generation (S_{H2O2}) as a function of the applied potential – see Fig. 2d and Table S1. The results obtained showed that, in general, all the catalysts exhibited high selectivity, with $S_{H2O2} > 82\%$; unsurprisingly, the Au-ZrO_2/PL6C catalyst exhibited the highest selectivity (~97%). Based on Fig S6, we obtained the results for the accelerated stress test (AST) conducted for Au-ZrO_2/PL6C. We noted a similar cycling profile of the material before and after AST, including preserving the same charge of the gold oxidation peak at ~0.8 V vs Ag/AgCl potential – which implies that no metal loss was recorded during the test. Furthermore, a similar behavior was observed for the disk and ring LSV curves before and after AST; this pointed to a high electrocatalytic stability of the Au-ZrO_2/PL6C when applied toward H_2O_2 production.

Thus, based on the physicochemical characterizations and electrochemical studies, we infer that the higher S_{H2O2} recorded for Au-ZrO_2/PL6C compared to Au/PL6C must be related to the reduced positive partial charge on gold NPs (caused by the donation of ZrO_2 electrons to the noble metal), which influences the interaction energy between Au and the adsorbed oxygen species. The optimal adsorption energy between Au and especially the *OOH intermediate results in the enhancement of the activity and selectivity toward H_2O_2. Apart from that, the favoring of *OOH destabilizes the formation of other intermediates, such as *O or *OH, which would lead to the production of H_2O.

The preliminary tests conducted using RRDE showed promising results related to the selectivity of the Au-ZrO_2/PL6C toward H_2O_2 production. The electrochemical behavior of the gold-based catalysts was also investigated based on the analysis of the kinetics of H_2O_2 accumulation in GDE. Fig. 2e shows the H_2O_2 production capacity profiles obtained for the different GDE modified materials investigated in this study. As can be observed, there was a gradual increase in H_2O_2 concentration over time, with the PL6C, ZrO_2/PL6C, Au/PL6C and Au-ZrO_2/PL6C GDEs recording approximately 140, 235, 374, and 600 mg L^{-1} H_2O_2 concentration, respectively, after 120 min of electrolysis. The pseudo zero-order kinetics for H_2O_2 production also indicated the superior catalytic performance of Au-ZrO_2/PL6C (0.19 s^{-1}), with 1.7 and 5-fold increase in kinetic efficiency compared to the Au/PL6C (0.11 s^{-1}) and the unmodified PL6C catalysts (0.04 s^{-1}). The improvement observed in Au-ZrO_2/PL6C in terms of H_2O_2 electrogeneration in the GDE setup is found to be in full agreement with the results obtained from the catalytic study conducted using the RRDE.

The current efficiency (CE) values obtained also pointed to the superior performance of the Au-ZrO_2/PL6C catalyst in terms of H_2O_2 production (Fig. S7 shows the CE profile over the electrolysis time). The comparative analysis of the CE values shown in Fig. 2f was performed using optimized values up to 20 min of reaction where there was low interference of H_2O_2 consumption reactions on the BDD anode. Looking at the results, it is clear that the highest H_2O_2 production efficiency obtained for the Au-ZrO_2/PL6C catalyst resulted from the CE of 70% recorded for the catalyst compared to 52% and > 50% CE recorded for the Au/PL6C and gold-free catalysts, respectively. As expected, the higher the CE of the catalyst employed in H_2O_2 production, the lower the energy consumption (EC) - see Fig. 2f. The PL6C catalyst recorded the highest EC in H_2O_2 production (with 105 kWh kg $(_{H2O2})^{-1}$) after 120 min of electrolysis, while the Au-ZrO_2/PL6C catalyst exhibited the lowest EC (with only 22 kWh kg $(_{H2O2})^{-1}$ - >80% decrease in consumption). The results obtained from the comparative analysis of the catalysts presented in Fig. 2f pointed to the following order of efficiency: Au-ZrO_2/PL6C > Au/PL6C > ZrO_2/PL6C > and PL6C.

In fact, a combination of the following factors was found to be responsible for the high catalytic activity and selectivity toward H_2O_2 electroproduction exhibited by the Au-ZrO_2/PL6C catalyst: i) the higher availability of active Au species on the ZrO_2/PL6C hybrid substrate (evidenced by the smaller particle size and high dispersibility of the Au NPs); ii) higher metal-support interaction — propelled by the higher electronegative character of Zr which supplies electrons so that Au becomes less oxidized; and iii) greater electron donation capacity of the Au centers prompted by the presence of ZrO_2 in the hybrid matrix (evidenced by the binding energy shift in the XPS analysis) compared to the Au/PL6C catalyst. Since Au-ZrO_2/PL6C exhibited the best electrocatalytic performance in terms of cathodic production of H_2O_2 among the catalysts investigated in this study, this catalyst was employed for the conduct of further tests using electrochemical systems for the removal of CBR based on the application of EAOPs.

3.3. CBR removal using H_2O_2-based EAOPs

Considering the promising results obtained from the application of

the Au-ZrO_2/PL6C catalyst for H_2O_2 production, the efficiency of the catalyst in the removal of CBR was tested based on the application of BDD as anode and different EAOPs with 10 mg L^{-1} CBR solution (at pH 2.5), at current density *(j)* of 50 mA cm^{-2} and temperature of 25 °C. Fig. 3a shows the decay of the CBR over time based on the application of the following treatment processes: UVC, AO, AO/H_2O_2, H_2O_2/UVC, EF and PEF.

First, the effect of CBR photolysis in the presence of UVC radiation resulted in a removal kinetics of 2.6 × 10^{-4} s^{-1} with only ~50% degradation of the compound after 60 min. Nevertheless, the photolysis process was found to exhibit very poor performance in terms of the mineralization of the organic compounds, recording only ~1% TOC removal; this may be attributed to radiation absorption of the compound in the 260–290 nm region, where it was able to degrade the CBR partially, but not mineralize it. The AO and AO-H_2O_2 processes exhibited poor electrochemical performance (see Fig. 3b), with pseudo-first order kinetics of 3.1 × 10^{-4} and 4.3 × 10^{-4} s^{-1} for CBR removal, respectively. In both techniques, the major contribution to the pollutant degradation was obtained from the heterogeneous $^{\bullet}$OH radicals produced on the BDD surface; this is clearly indicative of the low oxidizing power of H_2O_2 [72–74]. Under the AO-H_2O_2/UVC process, the total removal of CBR was obtained after approximately 20 min of treatment. Owing to the presence of UVC radiation in the AO-H_2O_2/UVC process (k_1 = 1.4 × 10^{-3} s^{-1}), the removal kinetics of this treatment technique was 2.6-fold higher compared to the AO/H_2O_2 process; this is attributed to the synergistic effect involving the contribution of UVC light in the production of homogeneous $^{\bullet}$OH from the photolysis of H_2O_2 and the photodegradation of carbaryl. The high efficiency of homogeneous $^{\bullet}$OH in the EF process contributed toward a rapid total removal of CBR in 10 min of treatment (k_1 = 3.5 × 10^{-2} s^{-1}). Thus, high production of H_2O_2 on the Au-ZrO_2/PL6C cathode enhances the production of $^{\bullet}$OH through both UVC radiation and Fenton reaction. As can be observed in Fig. 3c, the PEF process exhibited relatively faster kinetics with total CBR removal after only 4 min of treatment (k_1 = 4.1 × 10^{-2} s^{-1}); this behavior is attributed to the synergistic action involving the heterogeneous and homogeneous $^{\bullet}$OH processes, as well as the activation of H_2O_2 by UVC radiation and Fe^{2+} ions and the photodegradation of CBR.

Fig. 3d shows the mineralization rate for the processes investigated; the rate of mineralization was found to increase in the following order: AO (~32%) = AO/H_2O_2(~33%) < AO/H_2O_2/UVC (~49%) < EF (~57%) < PEF (~90%). Fig. 3d also shows that the processes with the lowest mineralization rates recorded the highest energy consumption values, though a higher efficient treatment made the process cheaper. In fact, it was noted that in 60 min of electrolysis, the AO process, which exhibited poor electrochemical mineralization, recorded an energy consumption of over 100 kWh (kg TOC)$^{-1}$. The PEF process was found to be more efficient in CBR mineralization compared to the EF process because the former involved additional UV light photodecarboxylation process (see Eq. (8)), which is found to promote further mineralization of Fe(III) complexes.

$$[Fe(OOCR)]^{2+} + hv \rightarrow Fe^{2+} + CO_2 + R^{\bullet} \quad (8)$$

The EF and PEF processes recorded quite similar *EC* values: 47.8 and 51.5 kWh kg $_{TOC}^{-1}$, respectively. Normally, irradiated processes exhibit a higher energy demand due to the use of UV lamp. However, these similar *EC* results were compensated by the faster mineralization rate exhibited by the PEF process.

Based on the optimal results obtained from the application of the Au-ZrO_2/PL6C catalyst in CBR removal under the PEF process, an analysis was carried out in order to evaluate under which conditions of current density and CBR concentration the system was able to sustain its high performance.

The removal of CBR normalized over time obtained from the application of different initial concentrations and current densities *(j)* are shown in Fig. 4a and b. The inset in Fig. 4 shows the pseudo-first order kinetics obtained for each parameter investigated. With regard to the different initial CBR concentrations, the application of the most diluted solution at 50 mA cm^{-2} led to the fastest removal of CBR, in less than 2 min of treatment (with k_1 = 8.1 × 10^{-2} s^{-1}). Solutions containing two or four times the initial concentration of CBR were still effectively treated, with total CBR removal obtained in 10 min of treatment (with k_1 values of 5.1 × 10^{-2} s^{-1} and 3.9 × 10^{-2} s^{-1}, respectively). All the TOC removal rates obtained at the end of 60 min of treatment were over 90% (see Table S2). We also noticed that the efficiency of the removal process decreases when there is lower concentration of CBR in the solution under investigation. The decrease in degradation efficiency observed in the presence of low concentration of the pollutant is attributed to some competitive reactions that occur among homogeneous oxidizing species,

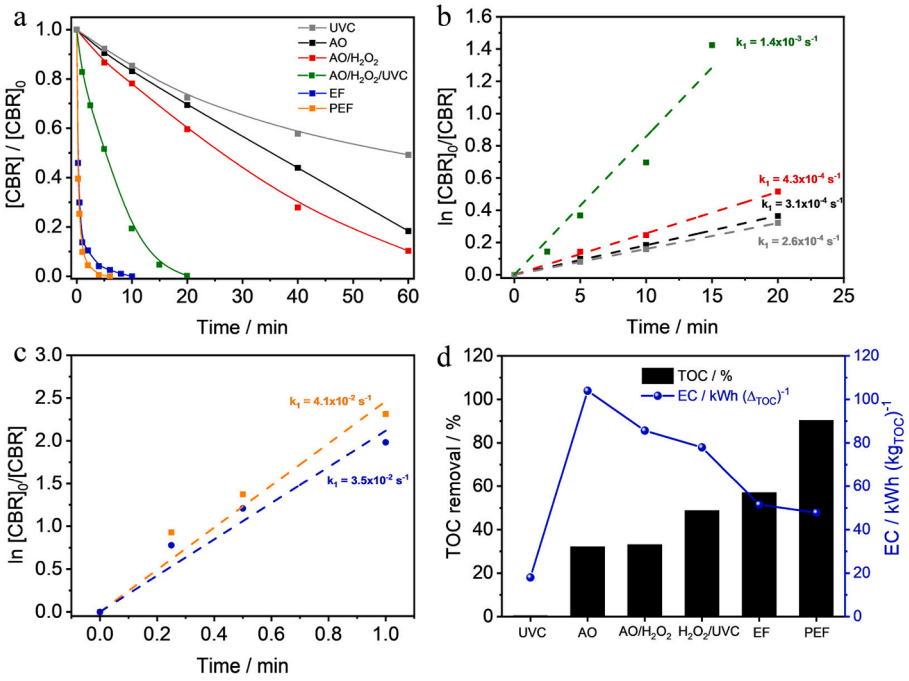

Fig. 3. (a)Analysis of the decay of 10 mg L^{-1} CBR based on the application of different electrochemical treatment processes. Pseudo-first order kinetics evaluated in acid medium composed of 0.1 mol L^{-1} K_2SO_4 (pH = 2.5), at current density (*j*) of 50 mA cm^{-2} for the following processes: (b) UVC, AO, AO/H_2O_2 and H_2O_2/UVC and (c) EF and PEF. (d) Profile of the percentage of mineralization in relation to energy consumption in kWh kg_{TOC}^{-1} obtained in 60 min of treatment based on the application of EAOPs with initial TOC of ~ 6.0 mg L^{-1}

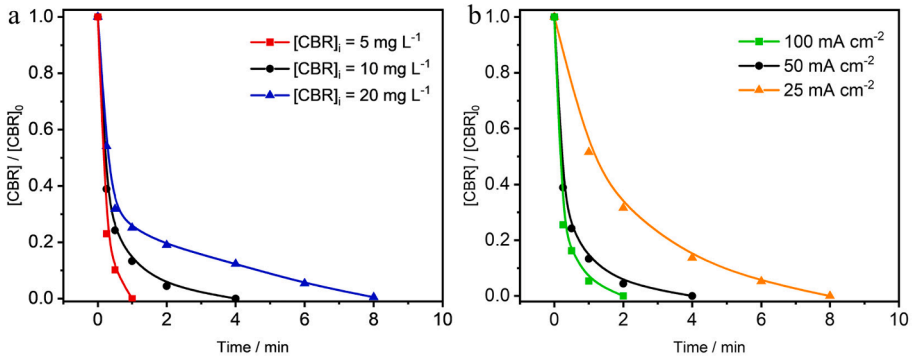

Fig. 4. (a) Analysis of the effect of initial CBR concentration using 5, 10 and 20 mg L^{-1} CBR concentrations, and (b) influence of applied current density *(j)* = 25, 50 and 100 mA cm^{-2} on the pollutant removal profile over time based on the application of 0.1 mol L^{-1} K_2SO_4 (pH 2.5) as electrolyte solution at j = 50 mA cm^{-2}.

which are found in excess in the solution (see Eq. (9), (10) and (11)), along with heterogeneous species that are formed on the anodic surface (see Eq. (12)) [75–78].

$$2^{\bullet}OH \rightarrow H_2O_2 \quad (9)$$

$$H_2O_2 + {}^{\bullet}OH \rightarrow HO_2^{\bullet} + H_2O \quad (10)$$

$$Fe^{2+} + {}^{\bullet}OH \rightarrow Fe^{3+} + OH^- \quad (11)$$

$$H_2O_2 + BDD(^{\bullet}OH) \rightarrow BDD(HO_2^{\bullet}) + H_2O \quad (12)$$

Moreover, limitations of mass transport between the pollutant, which presents low concentration gradient in solution, and the anodic surface can also reduce the efficiency of the electrochemical oxidation process. Thus, we understand that the degradation of low pollutant concentration has become one of the biggest challenges that need to be overcome in future studies when it comes to the application of electrochemical technologies for wastewater treatment [76].

Fig. 4b shows the results obtained from the analysis of the effect of current density on CBR degradation based on *j*-dependent kinetic profile. Presumably, the dependence of the applied current density on the degradation kinetics is related to both the cathodic production of H_2O_2 and the activation of $^{\bullet}OH$ adsorbed on the BDD anode; both phenomena are directly associated with the production of higher amount of $^{\bullet}OH$ (homogeneous or heterogeneous) which oxidizes both the CBR and its by-products. Thus, increasing the j from 25 ($k_1 = 1.0 \times 10^{-2}$ s^{-1}) to 50 mA cm^{-2} ($k_1 = 5.1 \times 10^{-2}$ s^{-1}) leads to a more efficient system, which is 5.1 times faster, when applied toward the removal of CBR. However, when the applied j is increased from 50 to 100 mA cm^{-2} ($k_1 = 6.6 \times 10^{-2}$ s^{-1}), the kinetics of CBR removal is found to increase by only 1.3 times; this increase is mostly derived from relatively faster thermodynamics which involves the production of H_2O by reducing the adsorbed H_2O_2 via a 2-electron plus pathway at very high current densities [22,79]. A comparative analysis of the TOC removal and energy consumption after 60 min of electrolysis (Table S2) enabled us to find the optimal current density to be applied in the electrochemical process. Thus, it was assumed that, up to the current density of 50 mA cm^{-2}, the system behaved in a very efficient manner in terms of CBR removal.

3.4. Identification of CBR by-products

During the oxidation process, the TOC removal data obtained under the PEF process pointed to a relative resistance to complete mineralization of the organic matter possibly due to the generation of stable by-products. The GC–MS analyses of the samples enabled us to identify the by-products generated along the mineralization pathway. The characteristics of the identified by-products, such as retention time and fragmentation (m/z), are presented in Table S3. The mineralization process proposed in Fig. 5 starts from the hydroxylation of carbaryl (1); this phenomenon yields the following compounds: 1-naphthyl (2) and 2-naphthyl (3), which, in turn, release methylcarbamic acid (the subsequent oxidation of methylcarbamic acid allows the production of further nitrogen species, apart from CO_2 and H_2O). Products 2 and 3 can be further hydroxylated to 1,4-naphthalene dione (4) or 1,2-naphthalene dione (5). The opening of the naphthalene ring leads to the production of phthalic acid (6), which can allow the loss of H_2O molecule to produce 2-carboxybenzaldehyde (7) or undergo multiple hydroxylations in order to produce catechol (8) and hydroquinone (9). Compounds 6, 7, 8, and 9 exhibit high oxidation state, and this leads to the generation of aliphatic organic compounds after the aromatic rings are fully opened – 1,2,3,4 butanetetracarboxylic acid (10), 3-(*tert*-butoxy)-3-oxopropanoic acid (11), and vinyl 2-ethylhexanoate (12).

Finally, the aliphatic organic compounds are hydroxylated to short-chain carboxylic acids. Generally, these carboxylic acids are highly efficient in producing Fe(III)-complexes ($[Fe(OOCR)]^{2+}$) in aqueous solution during electrochemical-Fenton based processes. Thus, the short-chain carboxylic acids were monitored by ion exchange high-performance liquid chromatography (HPLC). The short-chain acids identified were as follows: succinic acid (13), fumaric acid (14), malic acid (15), formic acid (16), acetic acid (17), and oxalic acid (18). The oxidation of CBR aromatic by-products led to an increase in the concentration of the acid in the first 40 min of treatment- see Fig. 6a. The short-chain acids were expected to be converted to oxalic acid - the most oxidized product, just before CO_2 production. The second plateau in the concentration of oxalic acid indicated the continued production of the acid after the mineralization process. The short-chain acids were completely transformed into CO_2 and H_2O after 120 min of treatment; this is in line with the 99% TOC removal rate obtained, except for the remnants of tiny amounts of formic and acetic acids.

As suggested, the oxidation of methylcarbamic acid yields nitrogen species as end-products of CBR mineralization. Thus, ion exchange HPLC was also employed for the monitoring of ammonium, nitrate, and nitrite species produced throughout the PEF process.

Fig. 6b shows that the main nitrogen ion species formed as the end-product of CBR mineralization was NO_3^-, with its maximum concentration of 0.46 mg L^{-1} obtained in 20 min of treatment. Despite the similarity in the profile of NO_3^- and NO_2^- production, the low NO_2^- concentration pointed to the highly oxidative power of the processes employed in the system. Interestingly, after reaching the maximum concentration in the first 20 min of electrolysis, we noted that the oxidized nitrogen species for NH_4^+ production were consumed; this phenomenon can be attributed to additional cathodic reaction of nitrite and nitrate reduction. Overall, the nitrogen content of all the ionic nitrogen species (N-NH_4^+, N-NO_2^- and N-NO_3^-) amounted to 0.62 mg L^{-1} after 120 min of treatment; i.e., 89% of the expected total nitrogen (0.7 mg L^{-1}) was identified through the mineralization of 10 mg L^{-1} of CBR. The incomplete mass balance can be explained by the production of nitrogen-based unidentified volatile species [80]. In brief, apart from it being highly efficient for H_2O_2 production targeted at the removal of

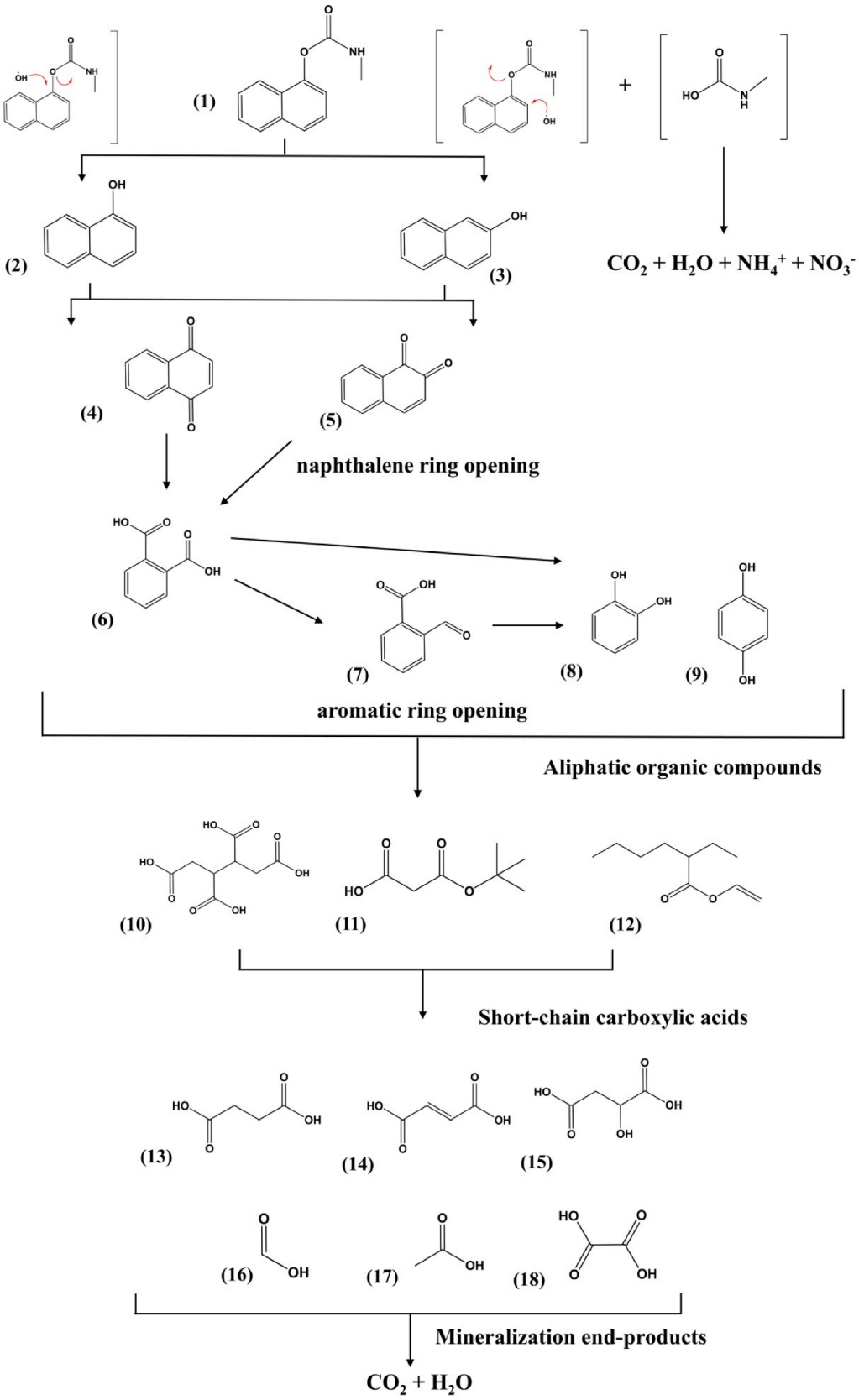

Fig. 5. Proposed route of carbaryl mineralization via hydroxyl radicals based on the application of PEF process in acid medium.

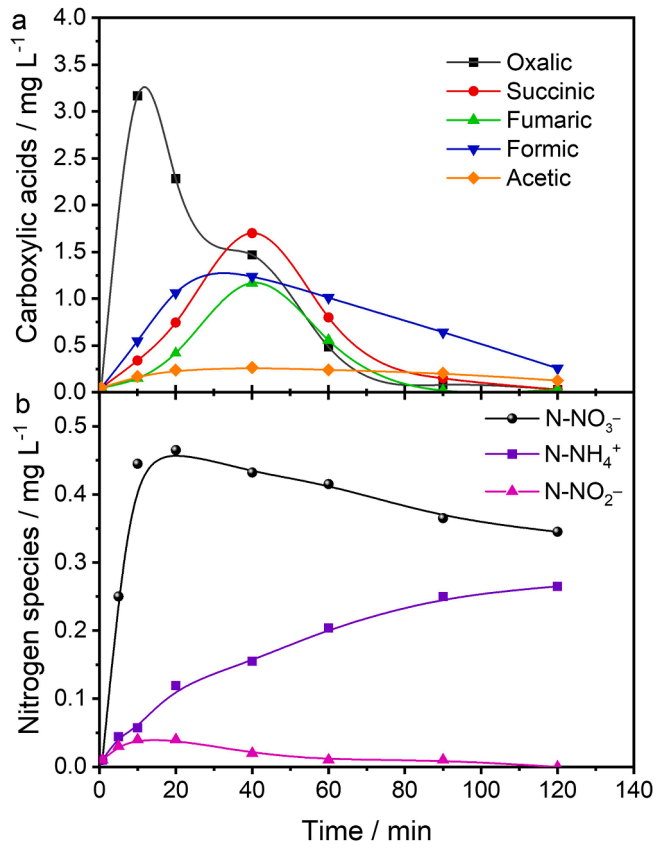

Fig. 6. Concentration of (a) small-chain carboxylic acids and (b) nitrogen species of NH_4^+, NO_3^- and NO_2^- identified during 120 min of 10 mg L^{-1} CBR degradation under the PEF process, based on the application of 150 mL of 0.1 mol L^{-1} K_2SO_4 (pH 2.5) as electrolyte and temperature of 25 °C.

CBR from water under the application of EAOPs, the Au NPs catalyst supported on ZrO_2/PL6C was also found to be a promising cathodic material for further environmental applications involving nitrate reduction.

3.5. Using pre-pilot plant for CBR removal in real urban wastewater

Although the study of electrochemical materials applied for the treatment of synthetic water matrices in lab scale is essentially important for developing mechanistic concepts, this approach does not contribute meaningfully toward improving and consolidating our scientific knowledge and understanding when it comes to real water treatment; this is because the extrapolations are often unrealistic when the analytical experiments are conducted in lab scale. This observation is supported by recent works related to applied electrochemical processes for the treatment of carbaryl outlined in Table S4; one will note that all the studies were performed in synthetic media and on a lab scale. Bearing that in mind, recent research in electrochemical technologies has been directed toward the use of real water matrices and scale-up processes [12,81,82]. Taking that into account, the present study conducted a series of experiments using urban wastewater spiked with CBR in an electrochemical flow reactor pre-pilot plant equipped with Au-ZrO_2/PL6C (cathode) and BDD (anode) - geometric area of both materials: 20 cm^{-2}. Additional details about the setup of the pre-pilot plant can be found in a paper recently published in the literature [83]. Fig. 7a shows that the amount of H_2O_2 generated in the wastewater treatment process was ~185 mg L^{-1} on average after performing five consecutive experiments at current density of 50 mA cm^{-2}. Further SEM images of the modified GDE (see Fig S8 of the supporting information) also showed a stable structure of the gold nanoparticles well distributed on the surface of the carbon oxide-based support after the H_2O_2 electrogeneration tests. Although the amount of H_2O_2 obtained was satisfactory for environmental water treatment, it was ~ 60% lower compared to the amount of H_2O_2 obtained in the synthetic medium under the same conditions; this can be attributed to the use of a flow reactor with a more realistic scale, as well as the presence of some compounds in the real medium, such as active chlorine species (Cl_2, HClO and ClO^-) derived

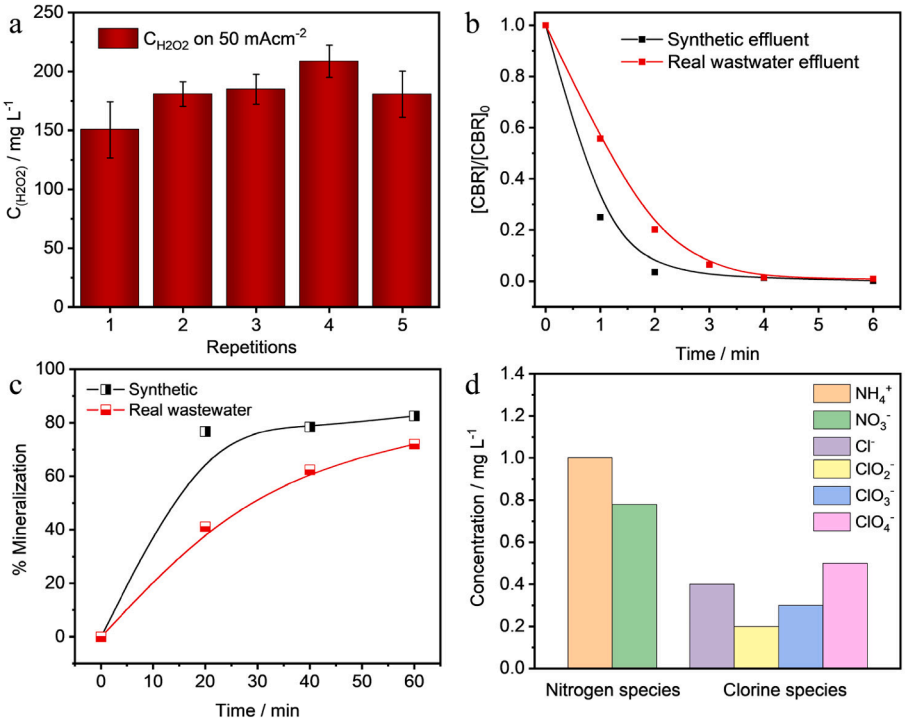

Fig. 7. (a) Stability tests related to H_2O_2 production in real wastewater effluent conducted with the aid of a flow reactor at applied current density *(j)* of 50 mA cm^{-2} using Au-ZrO_2/PL6C cathode and BDD anode. (b) Analysis of CBR removal and (c) TOC mineralization in flow electrochemical reactor based on the application of the PEF process at $j = 50$ mA cm^{-2} and O_2 flow at 100 mL min^{-1} in both synthetic and real effluents. (d) Final values of nitrogenous and chlorinated species detected in real wastewater effluent after 60 min of PEF treatment.

from Cl^- oxidation, which may act as H_2O_2 scavengers, as can be observed in Eqs. 13–15 [53,84].

$$H_2O_2 + Cl_2 \rightarrow O_2 + 2H^+ + 2Cl^- \quad (13)$$

$$H_2O_2 + HOCl \rightarrow O_2 + H_2O + H^+ + Cl^- \quad (14)$$

$$H_2O_2 + OCl^- \rightarrow O_2 + H_2O + Cl^- \quad (15)$$

For the analysis with real water, we tested the degradation of 10 mg L^{-1} CBR spiked in real urban wastewater. As can be observed in Fig. 7b, 78% of the pollutant was removed in 2 min of treatment. The degradation test conducted using synthetic water matrix and the same amount of time resulted in almost 96% of CBR removal. The compound was fully degraded in 4 min in both real and synthetic aqueous media. The values obtained for pseudo-first order kinetic constants showed that the degradation in the synthetic medium ($k_1 = 2.5 \times 10^{-2}\ s^{-1}$, $R^2 = 0.995$) occurred 1.6-fold faster than in the real medium ($k_1 = 1.6 \times 10^{-2}\ s^{-1}$, $R^2 = 0.986$). In addition, as can be observed in Fig. 7c, the mineralization process followed the same tendency; TOC removal of 82% was obtained under the synthetic medium as opposed to 71% obtained under the urban wastewater after 60 min of electrolysis. These results demonstrate that although the concentration of H_2O_2 electrogenerated in the real wastewater was lower than that generated in the synthetic medium, this did not inhibit the occurrence of Fenton reactions. It should be noted however that the presence of natural organic matter (NOM) affects the electrochemical system because these species compete with CBR for oxidants ($^{\bullet}OH$ and active chlorine species); this explains why lower CBR degradation was obtained under the real medium. From a mineralization point of view, the results obtained seem reasonable. This is because the initial TOC of the real medium (15.0 mg C L^{-1} = ~9.0 mg C L^{-1} from NOM + 6.0 mg C L^{-1} from CBR) was more than the double of that of the synthetic medium (containing only 6.0 mg C L^{-1} of CBR); thus, one would require a longer treatment time to obtain a complete mineralization of all the organic compounds present in the real medium. Furthermore, the residual TOC (4.4 mg C L^{-1}) in the real medium comes from NOM, which is more difficult to be mineralized than CBR. NOM is a complex mixture of organic compounds (humic acids, lipids, carbohydrates, etc.) which is derived from the breakdown of terrestrial plants and human activities [85].

Fig. 7d shows the final inorganic species left in the real medium after the electrochemical treatment. Active chloride species were converted into 0.20 mg L^{-1} of chlorite (ClO_2^-), 0.30 mg L^{-1} of chlorate (ClO_3^-) and 0.50 mg L^{-1} of perchlorate (ClO_4^-). Despite the generation of undesirable chlorine species (ClO_3^- and ClO_4^-), the concentrations of these species were found to be below the concentration limits established for the discharge of these compounds in wastewater (=10.0 mg L^{-1}). >80% of nitrogen species were removed. At the end of the electrochemical treatment process, 1.0 mg L^{-1} of NH_4^+ and 0.78 mg L^{-1} of NO_3^- were detected; this result points to the ability of the Au-ZrO_2/PL6C to effectively remove this kind of ions. With regard to the results obtained here, it is essentially important to note that before applying any type of process for the treatment of wastewater, one needs to characterize the medium thoroughly in order to verify what can influence the removal of the target pollutant.

4. Conclusion

This work investigated the synergistic relation between ZrO_2/PL6C support and Au NPs. The results obtained from the RRDE analysis conducted in the study showed that the anchoring of gold NPs on ZrO_2/PL6C hybrid support (Au-ZrO_2/PL6C) led to an increase in catalytic activity and selectivity toward H_2O_2 production (ORR onset = 0.34 V vs Ag/AgCl and S_{H2O2} = 97%) compared to the anchoring of Au particles on bare PL6C (ORR onset = 0.20 V vs Ag/AgCl and S_{H2O2} = 82%). The ZrO_2 species present in the Au-ZrO_2/PL6C catalyst, which is less electronegative than Au, helped supply electrons and favored the metallic state of Au NPs, which in turn boosted the catalytic activity toward H_2O_2 production.

The Au-ZrO_2/PL6C catalyst also displayed the best performance when applied in GDE, yielding an amount of 600 mgL^{-1} of H_2O_2 compared to ~374, ~235 and ~140 mgL^{-1} of H_2O_2 recorded for Au/PL6C, ZrO_2/PL6C, and bare PL6C, respectively. The performance of the Au-ZrO_2/PL6C cathodic catalyst in the removal of the endocrine interferent CBR was tested in an electrochemical cell coupled with BDD anode under the application of different EAOPs. The EF and PEF processes exhibited the highest efficiency in terms of CBR removal in less than 10 min of treatment; this outstanding efficiency was attributed to the significant production of homogeneous $^{\bullet}OH$ in the bulk solution through Fenton reaction. In addition, the PEF process, which exhibited a high mineralization percentage (>90%) in 60 min and energy consumption of 50.8 kWh kg^{-1}, was found to be the most efficient process for the treatment of CBR; the superior performance of the PEF process was attributed to the synergistic action involving $^{\bullet}OH$ activation via the Fenton reaction and UVC light, which occurs during the treatment process.

The tests conducted for the removal of CBR under different experimental conditions (j and [CBR]) showed that: i) the process efficiency decreases when lower concentration of CBR is applied; and ii) the application of higher current densities negatively affects the removal process due to the presence of non-negligible parallel/non-oxidizing reactions. Finally, a mineralization route was proposed based on TOC measurements coupled with the identification of aromatic degradation intermediates, short-chain acids, and ionic nitrogen species as the end-products of mineralization. The results obtained from the application of an electrochemical flow reactor at pre-pilot scale for the treatment of urban wastewater showed that the aqueous matrix influenced H_2O_2 electrogeneration and CBR degradation. Furthermore, at the end of the treatment process, the concentrations of inorganic species detected in the wastewater were found to be below the established discharge limit; this outcome pointed to the satisfactory efficiency of the process. Based on our findings, it can be concluded that the strategy proposed in this study, which involved the use of Au nanoparticles supported on ZrO_2/PL6C hybrid substrate, contributed effectively toward the cathodic production of H_2O_2 and the successful treatment of water containing complex matrices.

CRediT authorship contribution statement

Matheus S. Kronka: Investigation, Conceptualization, Methodology, Writing – original draft, Writing – review & editing. **Guilherme V. Fortunato:** Investigation, Conceptualization, Writing – original draft, Writing – review & editing. **Leticia Mira:** Methodology, Investigation, Writing – original draft. **Alexsandro J. dos Santos:** Investigation, Conceptualization, Writing – original draft, Writing – review & editing. **Marcos R.V. Lanza:** Supervision, Funding acquisition, Writing – review & editing.

Declaration of Competing Interest

The authors declare that they have no known competing financial interests or personal relationships that could have appeared to influence the work reported in this paper.

Data availability

Data will be made available on request.

Acknowledgments

The authors are grateful to the LCE/DEMa/UFSCar for providing the TEM facilities. The authors acknowledge the financial support provided by the following Brazilian research funding agencies: Brazilian National

Council for Scientific and Technological Development - CNPq (grant #465571/2014-0 and #303943/2021-1), São Paulo Research Foundation (FAPESP – grants #2014/50945-4, #2017/23464-3, #2017/10118-0, #2019/20634-0 and #2019/04421-7), and the Coordenação de Aperfeiçoamento de Pessoal de Nível Superior (CAPES – Finance Code 001).

Appendix A. Supplementary data

Supplementary data to this article can be found online at https://doi.org/10.1016/j.cej.2022.139598.

References

[1] J.R. Rohr, C.B. Barrett, D.J. Civitello, M.E. Craft, B. Delius, G.A. DeLeo, P. J. Hudson, N. Jouanard, K.H. Nguyen, R.S. Ostfeld, J.V. Remais, G. Riveau, S. H. Sokolow, D. Tilman, Emerging human infectious diseases and the links to global food production, Nat Sustain. 2 (2019) 445–456, https://doi.org/10.1038/s41893-019-0293-3.

[2] R.P. Schwarzenbach, T. Egli, T.B. Hofstetter, U. Von Gunten, B. Wehrli, Global water pollution and human health, Annu. Rev. Environ. Resour. 35 (2010) 109–136, https://doi.org/10.1146/annurev-environ-100809-125342.

[3] Food and Agriculture Organization of the United States (FAO), Pesticides Use, FAOSTAT. (2021). http://www.fao.org/faostat/en/#data/RP (accessed May 3, 2021).

[4] J. Safaa Noori, J. Mortensen, A. Geto, Recent Development on the Electrochemical Detection of Selected Pesticides: A Focused Review, Sensors 20 (2020) 2221, https://doi.org/10.3390/s20082221.

[5] J. Margot, L. Rossi, D.A. Barry, C. Holliger, A review of the fate of micropollutants in wastewater treatment plants, WIREs, Water 2 (2015) 457–487, https://doi.org/10.1002/wat2.1090.

[6] A.J. dos Santos, M.S. Kronka, G.V. Fortunato, M.R.V. Lanza, Recent advances in electrochemical water technologies for the treatment of antibiotics: A short review, Curr. Opin. Electrochem. 26 (2021), 100674, https://doi.org/10.1016/j.coelec.2020.100674.

[7] I. Sirés, E. Brillas, M.A. Oturan, M.A. Rodrigo, M. Panizza, Electrochemical advanced oxidation processes: Today and tomorrow. A review, Environ. Sci. Pollut. Res. 21 (2014) 8336–8367, https://doi.org/10.1007/s11356-014-2783-1.

[8] A.J. dos Santos, P.L. Cabot, E. Brillas, I. Sirés, A comprehensive study on the electrochemical advanced oxidation of antihypertensive captopril in different cells and aqueous matrices, Appl. Catal. B 277 (2020), 119240, https://doi.org/10.1016/j.apcatb.2020.119240.

[9] Z. Lang, M. Zhou, Q. Zhang, X. Yin, Y. Li, Comprehensive treatment of marine aquaculture wastewater by a cost-effective flow-through electro-oxidation process, Sci. Total Environ. 722 (2020), 137812, https://doi.org/10.1016/j.scitotenv.2020.137812.

[10] S. Chen, L. Tang, H. Feng, Y. Zhou, G. Zeng, Y. Lu, J. Yu, X. Ren, B. Peng, X. Liu, Carbon felt cathodes for electro-Fenton process to remove tetracycline via synergistic adsorption and degradation, Sci. Total Environ. 670 (2019) 921–931, https://doi.org/10.1016/j.scitotenv.2019.03.086.

[11] E. do Vale-Júnior, A.J. dos Santos, D.R. da Silva, A.S. Fajardo, C.A. Martínez-Huitle, Electrochemical technologies for detecting and degrading benzoquinone using diamond films, ChemElectroChem 6 (2019) 4383–4390, https://doi.org/10.1002/celc.201900541.

[12] E. Brillas, A review on the photoelectro-Fenton process as efficient electrochemical advanced oxidation for wastewater remediation. Treatment with UV light, sunlight, and coupling with conventional and other photo-assisted advanced technologies, Chemosphere 250 (2020), 126198, https://doi.org/10.1016/j.chemosphere.2020.126198.

[13] E. Brillas, I. Sirés, M.A. Oturan, Electro-fenton process and related electrochemical technologies based on fenton's reaction chemistry, Chem. Rev. 109 (2009) 6570–6631, https://doi.org/10.1021/cr900136g.

[14] A.J. dos Santos, E.C.T. de A. Costa, D.R. da Silva, S. Garcia-Segura, C.A. Martínez-Huitle, Electrochemical advanced oxidation processes as decentralized water treatment technologies to remediate domestic washing machine effluents, Environ. Sci. Pollut. Res. 25 (2018) 7002–7011, https://doi.org/10.1007/s11356-017-1039-2.

[15] M.A. Oturan, J.J. Aaron, Advanced oxidation processes in water/wastewater treatment: Principles and applications. A review, Crit. Rev. Environ. Sci. Technol. 44 (2014) 2577–2641, https://doi.org/10.1080/10643389.2013.829765.

[16] Z. Zhang, H. Meng, Y. Wang, L. Shi, X. Wang, S. Chai, Fabrication of graphene@graphite-based gas diffusion electrode for improving H_2O_2 generation in Electro-Fenton process, Electrochim. Acta 260 (2018) 112–120, https://doi.org/10.1016/j.electacta.2017.11.048.

[17] J. Wang, C. Li, M. Rauf, H. Luo, X. Sun, Y. Jiang, Gas diffusion electrodes for H_2O_2 production and their applications for electrochemical degradation of organic pollutants in water: A review, Sci. Total Environ. 759 (2021), 143459, https://doi.org/10.1016/j.scitotenv.2020.143459.

[18] P.J.M. Cordeiro-Junior, A.S. Martins, G.B.S. Pereira, F.V. Rocha, M.A.R. Rodrigo, M.R. de V. Lanza, Bisphenol-S removal via photoelectro-fenton/H_2O_2 process using Co-porphyrin/Printex L6 gas diffusion electrode, Sep. Purif. Technol. 285 (2022) 120299, https://doi.org/10.1016/j.seppur.2021.120299.

[19] L. Wang, J. Zhang, Y. Zhang, H. Yu, Y. Qu, J. Yu, Inorganic metal-oxide photocatalyst for H_2O_2 production, Small 18 (2022) 202104561, https://doi.org/10.1002/smll.202104561.

[20] E. Yeager, Electrocatalysts for O_2 reduction, Electrochim. Acta 29 (1984) 1527–1537, https://doi.org/10.1016/0013-4686(84)85006-9.

[21] P. Jorge Marques Cordeiro-Junior, M. Schiavon Kronka, L. Athie Goulart, N. Carolina Veríssimo, L. Helena Mascaro, M. Coelho dos Santos, R. Bertazzoli, M. Roberto de Vasconcelos Lanza, Catalysis of oxygen reduction reaction for H_2O_2 electrogeneration: The impact of different conductive carbon matrices and their physicochemical properties, J. Catal. 392 (2020) 56–68, https://doi.org/10.1016/j.jcat.2020.09.020.

[22] S. Yang, A. Verdaguer-Casadevall, L. Arnarson, L. Silvioli, V. Čolić, R. Frydendal, J. Rossmeisl, I. Chorkendorff, I.E.L. Stephens, Toward the Decentralized Electrochemical Production of H_2O_2: A Focus on the Catalysis, ACS Catal. 8 (2018) 4064–4081, https://doi.org/10.1021/acscatal.8b00217.

[23] J. An, Y. Feng, Q. Zhao, X. Wang, J. Liu, N. Li, Electrosynthesis of H_2O_2 through a two-electron oxygen reduction reaction by carbon based catalysts: From mechanism, catalyst design to electrode fabrication, Environ. Sci. Ecotechnol. 11 (2022), 100170, https://doi.org/10.1016/j.ese.2022.100170.

[24] G.O.S. Santos, P.J.M. Cordeiro-Junior, I. Sánchez-Montes, R.S. Souto, M.S. Kronka, M.R.V. Lanza, Recent advances in H_2O_2 electrosynthesis based on the application of gas diffusion electrodes: challenges and opportunities, Curr. Opin. Electrochem. (2022), 101124, https://doi.org/10.1016/j.coelec.2022.101124.

[25] I. Katsounaros, J.C. Meier, K.J.J.J. Mayrhofer, The impact of chloride ions and the catalyst loading on the reduction of H_2O_2 on high-surface-area platinum catalysts, Electrochim. Acta 110 (2013) 790–795, https://doi.org/10.1016/j.electacta.2013.03.156.

[26] G.V. Fortunato, E. Pizzutilo, E.S.F. Cardoso, M.R.V. Lanza, I. Katsounaros, S. J. Freakley, K.J.J. Mayrhofer, G. Maia, M. Ledendecker, The oxygen reduction reaction on palladium with low metal loadings: The effects of chlorides on the stability and activity towards hydrogen peroxide, J. Catal. 389 (2020) 400–408, https://doi.org/10.1016/j.jcat.2020.06.019.

[27] E. Pizzutilo, O. Kasian, C.H. Choi, S. Cherevko, G.J. Hutchings, K.J.J. Mayrhofer, S. J. Freakley, Electrocatalytic synthesis of hydrogen peroxide on Au-Pd nanoparticles: From fundamentals to continuous production, Chem. Phys. Lett. 683 (2017) 436–442, https://doi.org/10.1016/j.cplett.2017.01.071.

[28] L.B. Venarusso, J. Bettini, G. Maia, Catalysts for oxygen reduction reaction based on nanocrystals of a Pt or Pt–Pd alloy shell supported on a Au core, J. Solid State Electrochem. 20 (2016) 1753–1764, https://doi.org/10.1007/s10008-016-3181-z.

[29] G.A. Cerrón-Calle, T.P. Senftle, S. Garcia-Segura, Strategic tailored design of electrocatalysts for environmental remediation based on density functional theory (DFT) and microkinetic modeling, Curr. Opin. Electrochem. 35 (2022), 101062, https://doi.org/10.1016/j.coelec.2022.101062.

[30] H. Xu, D. Cheng, Y. Gao, Design of high-performance Pd-based alloy nanocatalysts for direct synthesis of H_2O_2, ACS Catal. 7 (2017) 2164–2170, https://doi.org/10.1021/acscatal.6b02871.

[31] J.S. Jirkovský, I. Panas, E. Ahlberg, M. Halasa, S. Romani, D.J. Schiffrin, Single atom hot-spots at Au–Pd nanoalloys for electrocatalytic H_2O_2 production, J. Am. Chem. Soc. 133 (2011) 19432–19441, https://doi.org/10.1021/ja206477z.

[32] S.J. Li, D. Bao, M.M. Shi, B.R. Wulan, J.M. Yan, Q. Jiang, Amorphizing of Au nanoparticles by CeOx–RGO Hybrid support towards highly efficient electrocatalyst for N2 reduction under ambient conditions, Adv. Mater. 29 (2017) 1700001, https://doi.org/10.1002/adma.201700001.

[33] Y. Du, H. Sheng, D. Astruc, M. Zhu, Atomically precise noble metal nanoclusters as efficient catalysts: a bridge between structure and properties, Chem. Rev. 120 (2020) 526–622, https://doi.org/10.1021/acs.chemrev.8b00726.

[34] V. Viswanathan, H.A. Hansen, J. Rossmeisl, J.K. Nørskov, Unifying the 2e - and 4e - reduction of oxygen on metal surfaces, J. Phys. Chem. Lett. 3 (2012) 2948–2951, https://doi.org/10.1021/jz301476w.

[35] G.V. Fortunato, M.S. Kronka, A.J. dos Santos, M. Ledendecker, M.R.V. Lanza, Low Pd loadings onto Printex L6: Synthesis, characterization and performance towards H2O2 generation for electrochemical water treatment technologies, Chemosphere 259 (2020), 127523, https://doi.org/10.1016/j.chemosphere.2020.127523.

[36] D. Gogoi, A. Namdeo, A.K. Golder, N.R. Peela, Ag-doped TiO2 photocatalysts with effective charge transfer for highly efficient hydrogen production through water splitting, Int. J. Hydrogen Energy 45 (2020) 2729–2744, https://doi.org/10.1016/J.IJHYDENE.2019.11.127.

[37] V.S. Antonin, L.S. Parreira, L.R. Aveiro, F.L. Silva, R.B. Valim, P. Hammer, M.R. V. Lanza, M.C. Santos, W@Au nanostructures modifying carbon as materials for hydrogen peroxide electrogeneration, Electrochim. Acta 231 (2017) 713–720, https://doi.org/10.1016/j.electacta.2017.01.192.

[38] L.C. Trevelin, R.B. Valim, J.F. Carneiro, A. de Siervo, R.S. Rocha, M.R.V. Lanza, Using black carbon modified with NbMo and NbPd oxide nanoparticles for the improvement of H_2O_2 electrosynthesis, J. Electroanal. Chem. 877 (2020), 114746, https://doi.org/10.1016/j.jelechem.2020.114746.

[39] G.V. Fortunato, L.S. Bezerra, E.S.F. Cardoso, M.S. Kronka, A.J. Santos, A.S. Greco, J.L.R.J. Júnior, M.R.V. Lanza, G. Maia, Using palladium and gold palladium nanoparticles decorated with molybdenum oxide for versatile hydrogen peroxide electroproduction on graphene nanoribbons, ACS Appl. Mater. Interfaces. 14 (2022) 6793, https://doi.org/10.1021/acsami.1c22362.

[40] J.F. Carneiro, L.C. Trevelin, A.S. Lima, G.N. Meloni, M. Bertotti, P. Hammer, R. Bertazzoli, M.R.V. Lanza, Synthesis and characterization of ZrO_2/C as electrocatalyst for oxygen reduction to H_2O_2, Electrocatalysis. 8 (2017) 189–195, https://doi.org/10.1007/s12678-017-0355-0.

[41] J.F. Carneiro, F.L. Silva, A.S. Martins, R.M.P. Dias, G.M. Titato, Á.J. Santos-Neto, R. Bertazzoli, M.R.V. Lanza, Simultaneous degradation of hexazinone and diuron

using ZrO_2-nanostructured gas diffusion electrode, Chem. Eng. J. 351 (2018) 650–659, https://doi.org/10.1016/j.cej.2018.06.122.
[42] M.S. Kronka, P.J.M. Cordeiro-Junior, L. Mira, A.J. dos Santos, G.V. Fortunato, M.R. V. Lanza, Sustainable microwave-assisted hydrothermal synthesis of carbon-supported ZrO_2 nanoparticles for H_2O_2 electrogeneration, Mater. Chem. Phys. 267 (2021), https://doi.org/10.1016/j.matchemphys.2021.124575.
[43] A.J. dos Santos, S. Garcia-Segura, S. Dosta, I.G. Cano, C.A. Martínez-Huitle, E. Brillas, A ceramic electrode of ZrO2-Y2O3 for the generation of oxidant species in anodic oxidation. Assessment of the treatment of Acid Blue 29 dye in sulfate and chloride media, in: Sep. Purif. Technol., 228, 2019, p. 115747, https://doi.org/10.1016/j.seppur.2019.115747.
[44] Z. Azdad, L. Marot, L. Moser, R. Steiner, E. Meyer, Valence band behaviour of zirconium oxide, Photoelectron and Auger spectroscopy study, Sci. Rep. 8 (2018) 1–6, https://doi.org/10.1038/s41598-018-34570-w.
[45] A.O. Docea, E. Gofita, M. Goumenou, D. Calina, O. Rogoveanu, M. Varut, C. Olaru, E. Kerasioti, P. Fountoucidou, I. Taitzoglou, O. Zlatian, V.N. Rakitskii, A. F. Hernandez, D. Kouretas, A. Tsatsakis, Six months exposure to a real life mixture of 13 chemicals' below individual NOAELs induced non monotonic sex-dependent biochemical and redox status changes in rats, Food Chem. Toxicol. 115 (2018) 470–481, https://doi.org/10.1016/j.fct.2018.03.052.
[46] E.H. Criteria, Environmental Health Criteria 153, Environmental Health Criteria, Carbaryl, 1994, pp. 1–358.
[47] P. Spirhanzlova, J.B. Fini, B. Demeneix, S. Lardy-Fontan, S. Vaslin-Reimann, B. Lalere, N. Guma, A. Tindall, S. Krief, Composition and endocrine effects of water collected in the Kibale national park in Uganda, Environ. Pollut. 251 (2019) 460–468, https://doi.org/10.1016/j.envpol.2019.05.006.
[48] G.V. Fortunato, E. Pizzutilo, A.M. Mingers, O. Kasian, S. Cherevko, E.S.F. Cardoso, K.J.J. Mayrhofer, G. Maia, M. Ledendecker, Impact of palladium loading and interparticle distance on the selectivity for the oxygen reduction reaction toward hydrogen peroxide, J. Phys. Chem. C. 122 (2018) 15878–15885, https://doi.org/10.1021/acs.jpcc.8b04262.
[49] U.A. Paulus, T.J. Schmidt, H.A. Gasteiger, R.J. Behm, Oxygen reduction on a high-surface area Pt/Vulcan carbon catalyst: A thin-film rotating ring-disk electrode study, J. Electroanal. Chem. 495 (2001) 134–145, https://doi.org/10.1016/S0022-0728(00)00407-1.
[50] J. Moreira, V. Bocalon Lima, L. Athie Goulart, M.R.V. Lanza, Electrosynthesis of hydrogen peroxide using modified gas diffusion electrodes (MGDE) for environmental applications: Quinones and azo compounds employed as redox modifiers, Appl. Catal. B 248 (2019) 95–107, https://doi.org/10.1016/j.apcatb.2019.01.071.
[51] R.B. Valim, R.M. Reis, P.S. Castro, A.S. Lima, R.S. Rocha, M. Bertotti, M.R.V. Lanza, Electrogeneration of hydrogen peroxide in gas diffusion electrodes modified with tert-butyl-anthraquinone on carbon black support, Carbon N Y. 61 (2013) 236–244, https://doi.org/10.1016/j.carbon.2013.04.100.
[52] M.S. Çelebi, N. Oturan, H. Zazou, M. Hamdani, M.A. Oturan, Electrochemical oxidation of carbaryl on platinum and boron-doped diamond anodes using electro-Fenton technology, Sep. Purif. Technol. 156 (2015) 996–1002, https://doi.org/10.1016/j.seppur.2015.07.025.
[53] A.J. dos Santos, A.S. Fajardo, M.S. Kronka, S. Garcia-Segura, M.R.V. Lanza, Effect of electrochemically-driven technologies on the treatment of endocrine disruptors in synthetic and real urban wastewater, Electrochim. Acta 376 (2021), 138034, https://doi.org/10.1016/j.electacta.2021.138034.
[54] Nanometal, in: Fundamentals and Applications of Nano Silicon in Plasmonics and Fullerines, Elsevier, 2018: pp. 169–203. doi: 10.1016/b978-0-323-48057-4.00008-6.
[55] B. Zhang, L. Fan, H. Zhong, Y. Liu, S. Chen, Graphene nanoelectrodes: fabrication and size-dependent electrochemistry, J. Am. Chem. Soc. 135 (2013) 10073–10080, https://doi.org/10.1021/ja402456b.
[56] M. Ledendecker, S. Geiger, K. Hengge, J. Lim, S. Cherevko, A.M. Mingers, D. Göhl, G.V. Fortunato, D. Jalalpoor, F. Schüth, C. Scheu, K.J.J. Mayrhofer, Towards maximized utilization of iridium for the acidic oxygen evolution reaction, Nano Res. 12 (2019) 2275–2280, https://doi.org/10.1007/s12274-019-2383-y.
[57] S. Guo, S. Zhang, S. Sun, Tuning nanoparticle catalysis for the oxygen reduction reaction, Angew. Chem. Int. Ed. Engl. 52 (2013) 2–21, https://doi.org/10.1002/anie.201207186.
[58] F. Banhart, Interactions between metals and carbon nanotubes: at the interface between old and new materials, Nanoscale. 1 (2009) 201, https://doi.org/10.1039/b9nr00127a.
[59] L. Xin, F. Yang, S. Rasouli, Y. Qiu, Z.F. Li, A. Uzunoglu, C.J. Sun, Y. Liu, P. Ferreira, W. Li, Y. Ren, L.A. Stanciu, J. Xie, Understanding Pt nanoparticle anchoring on graphene supports through surface functionalization, ACS Catal. 6 (2016) 2642–2653, https://doi.org/10.1021/acscatal.5b02722.
[60] M.A. Asadabad, M.J. Eskandari, Transmission Electron Microscopy as Best Technique for Characterization in Nanotechnology, Synth. React. Inorg. Met.-Org. Nano-Met. Chem 45 (2015) 323–326, https://doi.org/10.1080/15533174.2013.831901.
[61] L.B. Venarusso, J. Bettini, G. Maia, Superior catalysts for oxygen reduction reaction based on porous nanostars of a Pt, Pd, or Pt-Pd alloy shell supported on a gold core, ChemElectroChem 3 (2016) 749–756, https://doi.org/10.1002/celc.201600046.
[62] B. Donoeva, N. Masoud, P.E. de Jongh, Carbon support surface effects in the gold-catalyzed oxidation of 5-hydroxymethylfurfural, ACS Catal. 7 (2017) 4581–4591, https://doi.org/10.1021/acscatal.7b00829.
[63] J.T. Miller, A.J. Kropf, Y. Zha, J.R. Regalbuto, L. Delannoy, C. Louis, E. Bus, J. A. van Bokhoven, The effect of gold particle size on Au-Au bond length and reactivity toward oxygen in supported catalysts, J. Catal. 240 (2006) 222–234, https://doi.org/10.1016/j.jcat.2006.04.004.
[64] J.S. Jirkovský, M. Halasa, D.J. Schiffrin, Kinetics of electrocatalytic reduction of oxygen and hydrogen peroxide on dispersed gold nanoparticles, PCCP 12 (2010) 8042–8052, https://doi.org/10.1039/c002416c.
[65] M. Chen, D. Kumar, C.-W. Yi, D.W. Goodman, The promotional effect of gold in catalysis by palladium-gold, Science 310 (2005) 291–293, https://doi.org/10.1126/science.1115800.
[66] J.K. Edwards, S.J. Freakley, R.J. Lewis, J.C. Pritchard, G.J. Hutchings, Advances in the direct synthesis of hydrogen peroxide from hydrogen and oxygen, Catal. Today 248 (2015) 3–9, https://doi.org/10.1016/j.cattod.2014.03.011.
[67] R.J. White, R. Luque, V.L. Budarin, J.H. Clark, D.J. Macquarrie, Supported metal nanoparticles on porous materials. Methods and applications, Chem. Soc. Rev. 38 (2009) 481–494, https://doi.org/10.1039/B802654H.
[68] S. Navalon, A. Dhakshinamoorthy, M. Alvaro, M. Antonietti, H. García, Active sites on graphene-based materials as metal-free catalysts, Chem. Soc. Rev. 46 (2017) 4501–4529, https://doi.org/10.1039/c7cs00156h.
[69] G.V. Fortunato, F. de Lima, G. Maia, Oxygen-reduction reaction strongly electrocatalyzed by Pt electrodeposited onto graphene or graphene nanoribbons, J. Power Sources 302 (2016) 247–258, https://doi.org/10.1016/j.jpowsour.2015.10.069.
[70] D. Aranzales, J.H.O.J. Wijenberg, M.T.M. Koper, Voltammetric study of tin electrodeposition on polycrystalline gold from sulfuric and methanesulfonic acid, J. Electrochem. Soc. 166 (2019) D283–D289, https://doi.org/10.1149/2.0211908jes.
[71] E.E. Benn, B. Gaskey, J.D. Erlebacher, Suppression of hydrogen evolution by oxygen reduction in nanoporous electrocatalysts, J. Am. Chem. Soc. 139 (2017) 3663–3668, https://doi.org/10.1021/JACS.6B10855.
[72] S. Vasilie, F. Manea, A. Baciu, A. Pop, Dual use of boron-doped diamond electrode in antibiotics-containing water treatment and process control, Process Saf. Environ. Prot. 117 (2018) 446–453, https://doi.org/10.1016/j.psep.2018.05.024.
[73] S.O. Ganiyu, C.A. Martínez-Huitle, M.A. Oturan, Electrochemical advanced oxidation processes for wastewater treatment: Advances in formation and detection of reactive species and mechanisms, Curr. Opin. Electrochem. 27 (2021), 100678, https://doi.org/10.1016/j.coelec.2020.100678.
[74] A.S. Fajardo, A.J. dos Santos, E.C.T. de Araújo Costa, D.R. da Silva, C.A. Martínez-Huitle, Effect of anodic materials on solar photoelectro-Fenton process using a diazo dye as a model contaminant, Chemosphere 225 (2019) 880–889, https://doi.org/10.1016/j.chemosphere.2019.03.071.
[75] A.A. Márquez, I. Sirés, E. Brillas, J.L. Nava, Mineralization of Methyl Orange azo dye by processes based on H_2O_2 electrogeneration at a 3D-like air-diffusion cathode, Chemosphere 259 (2020), 127466, https://doi.org/10.1016/j.chemosphere.2020.127466.
[76] S. Garcia-Segura, X. Qu, P.J.J. Alvarez, B.P. Chaplin, W. Chen, J.C. Crittenden, Y. Feng, G. Gao, Z. He, C.H. Hou, X. Hu, G. Jiang, J.H. Kim, J. Li, Q. Li, J. Ma, J. Ma, A.B. Nienhauser, J. Niu, B. Pan, X. Quan, F. Ronzani, D. Villagran, T. D. Waite, W.S. Walker, C. Wang, M.S. Wong, P. Westerhoff, Opportunities for nanotechnology to enhance electrochemical treatment of pollutants in potable water and industrial wastewater-a perspective, Environ. Sci. Nano 7 (2020) 2178–2194, https://doi.org/10.1039/d0en00194e.
[77] S.O. Ganiyu, E. Vieira dos Santos, E.C. Tossi de Araújo Costa, C.A. Martínez-Huitle, Electrochemical advanced oxidation processes (EAOPs) as alternative treatment techniques for carwash wastewater reclamation, Chemosphere 211 (2018) 998–1006, https://doi.org/10.1016/j.chemosphere.2018.08.044.
[78] M. Brienza, S. Garcia-Segura, Electrochemical oxidation of fipronil pesticide is effective under environmental relevant concentrations, Chemosphere 307 (2022), 135974, https://doi.org/10.1016/j.chemosphere.2022.135974.
[79] C.H. Choi, H.C. Kwon, S. Yook, H. Shin, H. Kim, M. Choi, Hydrogen peroxide synthesis via enhanced two-electron oxygen reduction pathway on carbon-coated pt surface, J. Phys. Chem. C 118 (2014) 30063–30070, https://doi.org/10.1021/jp5113894.
[80] I. Katsounaros, On the assessment of electrocatalysts for nitrate reduction, Curr. Opin. Electrochem. 28 (2021), 100721, https://doi.org/10.1016/j.coelec.2021.100721.
[81] S. Garcia-Segura, A.B. Nienhauser, A.S. Fajardo, R. Bansal, C.L. Coonrod, J. D. Fortner, M. Marcos-Hernández, T. Rogers, D. Villagran, M.S. Wong, P. Westerhoff, Disparities between experimental and environmental conditions: Research steps toward making electrochemical water treatment a reality, Curr. Opin. Electrochem. 22 (2020) 9–16, https://doi.org/10.1016/j.coelec.2020.03.001.
[82] C.A. Martínez-Huitle, M.A. Rodrigo, I. Sirés, O. Scialdone, Single and coupled electrochemical processes and reactors for the abatement of organic water pollutants: A critical review, Chem. Rev. 115 (2015) 13362–13407, https://doi.org/10.1021/acs.chemrev.5b00361.
[83] A.J.M. da Costa, M.S. Kronka, P.J.M. Cordeiro-Junior, G.V. Fortunato, A.J. dos Santos, M.R.V. Lanza, Treatment of Tebuthiuron in synthetic and real wastewater using electrochemical flow-by reactor, J. Electroanal. Chem. 882 (2021), 114978, https://doi.org/10.1016/j.jelechem.2021.114978.
[84] J.R. Steter, E. Brillas, I. Sirés, On the selection of the anode material for the electrochemical removal of methylparaben from different aqueous media, Electrochim. Acta 222 (2016) 1464–1474, https://doi.org/10.1016/j.electacta.2016.11.125.
[85] A. Serrà, L. Philippe, F. Perreault, S. Garcia-Segura, Photocatalytic treatment of natural waters. Reality or hype? The case of cyanotoxins remediation, Water Res. 188 (2021), 116543, https://doi.org/10.1016/j.watres.2020.116543.